DEVELOPMENT OF A LIQUID DRUG DELIVERY PAYLOAD FOR MODULAR, WIRELESS, INCORPOREAL ROBOTS FOR LAPAROSCOPIC SURGERY

BY

JACOB KUNOWSKI

THESIS

Submitted in partial fulfillment of the requirements
for the degree of Master of Science in Mechanical Engineering
in the Graduate College of the
University of Illinois at Urbana-Champaign, 2010

Urbana, Illinois

Adviser:

Professor Stephen R. Platt

Abstract

Minimally invasive abdominal surgery (laparoscopy) is performed using long, slender instruments inserted through multiple small incisions in the patient's abdominal wall. This results in less post–operative pain, shorter hospital stays, and a quicker return to normal activities for the patient compared to conventional open surgery; however, the use of small entry incisions provides only limited access to the surgical site compared to conventional open surgery. Robotic systems have been developed that overcome some limitations with laparoscopic surgery. The systems, however, are very high cost, provide limited benefit to the patient, and do not completely address limited access issues and the need for multiple incisions. New techniques, such as single–port laparoscopic and natural orifice surgery, reduce the number of entry incisions but still provide only limited access to the surgical site. An innovative solution that potentially overcomes both limitations is to insert miniature robotic assistants entirely inside the abdominal cavity through a single incision where they can be readily relocated as needed. Previous work has demonstrated that a family of fixed–base and modular, wireless, intracorporeal, mobile robots can successfully monitor physiological conditions, perform biopsies, staple and clamp tissue, and provide visual feedback within the abdominal cavity. Current robots do not have the ability to store or dispense liquids such as hemostatic agents. The use of hemostatic agents, such as fibrin sealants, instead of mechanical or electrical means of hemostasis alleviates the extensive training required for laparoscopic suturing, the nerve damage accompanying staples or tacks, and the need for a relatively large energy source for electrocautery tools and harmonic scalpels. An incorporeal robot capable of carrying and delivering liquids would combine the advantages of incorporeal mobile robots and liquid hemostatic agents. The main focus of this thesis is the development of a liquid delivery payload for a family of incorporeal robotic assistants. Included

in this development is a method for mixing two liquids stored inside the robot as they are dispensed, which is needed for dual compound liquids such as fibrin sealants. Finally, two improvements to the design of the control electronics are presented that allow for more rapid robot deployment and provide the ability for point of use changes to the embedded control software.

Dedicated to Candice. Without her love, continuous support, and inspiration, none of this would have been possible.

Acknowledgments

I would like to sincerely thank my adviser Professor Stephen R. Platt for allowing me to work on such an interesting research topic. His excellent guidance and encouragement throughout my time as a graduate student will continue to help me be successful in my professional career. Thank you to Jeff Hawks and Mark Rentschler for their assistance with porcine model testing.

I would also like to thank Bob Coverdill for all of his help creating rapid prototyped parts, Dan Block for his advice with printed circuit board design, and Dr. Wanhong Yang for his coaching with computer simulation. Dr. Wanhong Yang's mentoring has taught me skills to help me be successful in my personal and professional lives.

I am especially grateful for all of the backing and encouragement from my family.

Table of Contents

Chapter 1

Background on Minimally Invasive Surgery

Various robotic systems developed in the 1990s were designed to help in minimally invasive surgery, a type of surgery where in which incisions are made in a patient's body, instead of the long incisions associated with conventional surgery that require many stitches to close and often result in a long recovery time for the patient. A familiar example of minimally invasive surgery is the laparoscopic appendectomy–removal of an appendix through a small incision made near the belly button. Although current robotic systems used in minimally invasive surgery are greatly improved over the earlier systems, they still require multiple incisions and provide only limited access to the surgical site. For this thesis, three modifications to a system of intracorporeal, miniature, surgical robotic devices were designed and tested to address the need for a liquid drug delivery payload, improved power management, and more rapid embedded software updates. The main modification involved the development and testing of a liquid drug delivery payload. The two other modifications involved changes to the robot main circuit board to allow turning the robot on or off from the exterior of the robot body using a magnet and to provide the ability for point of use changes to the embedded control software. Chapters 1–4 of the thesis provide background information on minimally invasive surgery, intracorporeal robotic systems, hemostatic techniques, and liquid mixing devices. Chapters 5–9 discuss the development and testing of the liquid drug delivery payload. Chapter 10 discusses the development of the two improvements to the robot main control board.

1.1 Minimally Invasive Surgery

Minimally invasive surgery (MIS) involves medical procedures performed through one or more short incisions. This is in contrast to one long incision typically used in open surgery [1]. Using one or more short incisions is beneficial because it results in reduced patient trauma and morbidity, and allows for more rapid recovery compared to conventional surgery [1]–[3]. Laparoscopic surgery is MIS in the abdominal cavity using slender, long instruments for tissue manipulation and an endoscope for visualization of the surgical environment. The advantages of laparoscopic procedures over conventional procedures are less post–operative pain, shorter hospital stays, and quicker return to normal activities [4]–[6]. For example, patients who undergo laparoscopic appendectomy, cholecystectomy (gall bladder removal), antireflux surgery, or gastric bypass surgery are 72% less likely to experience surgical–site infections than those who undergo an open procedure [7].

Even though laparoscopic procedures have many advantages for the patient, one disadvantage for the surgeon is the limited access to the surgical site provided by the use of small entry incisions and one disadvantage for the patient is the need to use multiple incisions for a procedure. The limited access to the surgical site results in reduced perception, dexterity, and degrees of motion for the surgeon compared to conventional open surgery [8]. Because multiple incisions are used for a procedure, there is opportunity to further reduce patient trauma by reducing the number of incisions.

Procedures such as single–port laparoscopic surgery and natural orifice surgery are being developed to reduce the number of entry incisions made in the abdominal wall; however, these approaches still do not address limited access to the surgical site. To help return lost perception, dexterity, and degrees of motion to the surgeon in laparoscopic surgery, improved tools and robotic assistants are being developed.

1.2 Improvements to Laparoscopic Surgery

1.2.1 Single–Port Laparoscopic Surgery

Laparoscopic techniques can vary widely but multiple small incisions are commonly made to complete a procedure. An endoscope is inserted through one incision while other instruments such as graspers or scissors use other ports [1]. An emerging concept is single–port or single–incision laparoscopic surgery. To reduce the trauma to surrounding tissue compared to conventional laparoscopy, all of the laparoscopic instruments enter the abdominal cavity through the same incision [9]. Most current devices designed to facilitate single–port laparoscopy consist of a large sheath containing multiple ports for insertion of laparoscopic instruments [9]. The sheath is placed through the incision that is usually located at the umbilicus.

Surgeons undergo additional training and need to learn new techniques for single–port laparoscopic surgery versus conventional laparoscopic surgery. Because multiple instruments are inserted through a relatively short incision, a significant portion of the learning curve is dedicated to placement of the surgeon's hands [9]. Some solutions to this problem include using articulated instruments, rotating instrument handles, variable length instruments, and tools with multiple end–effectors [9]. However, these solutions are still constrained by the small entry incision.

1.2.2 Natural Orifice Surgery

A technique in development aimed at completely eliminating abdominal wall incisions is natural orifice translumenal endoscopic surgery (NOTES). NOTES is a MIS technique in which a flexible endoscope is passed through the mouth, anus, urethra, or vagina to gain access to the abdominal cavity [10]. For example, in a cholecystectomy, a surgeon would insert a tube through the mouth and down the esophagus, make an incision in the stomach or digestive tract, locate and cut the gallbladder, and remove it through the mouth [11]. NOTES is still in the early stages of investigation but it offers the possibility of being performed without general anesthesia because no skin incisions are made and the tools

and equipment are portable and require only high–level disinfection instead of sterilization [10]. However, this technique is not yet clinically relevant and still uses a laparoscopic port to determine if the procedure can be performed safely. For example, a clinical study of 14 NOTES operations identified that three cases abandoned a NOTES approach because severe inflammation or adhesion was found during the initial examination through a laparoscopic port [12]. Limited access to the surgical site is also still present in NOTES because the endoscope is passed through a natural orifice.

1.2.3 Improved Tools

Next generation robotics are currently being developed that improve mobility and reduce complexity and cost. For example, a prototype laparoscopic robot has been built and tested by the Medical Robotics Group at the University of California–Berkeley that provides force and tactile feedback for telesurgical applications [13], [14]. Intelligent microsurgical instruments that electronically cancel tremor in handheld surgical tools are being developed by the Carnegie Mellon University's Robotics Institute [15], [16]. Also, at the Bio–Robotics Laboratory at the University of Washington, new endoscopic tools with force and tactile feedback are being developed [17]. However, these devices are still limited by the entry incisions and do not reduce the number of required incisions in the abdominal wall.

1.2.4 Robotic Systems

The use of robotic systems in surgery has helped to increase the surgeon's perception, dexterity, and degrees of freedom compared to conventional MIS. LARS and AESOP were the first robotic systems developed during the 1990s to assist during minimally invasive abdominal surgery [18], [19]. Currently, the da Vinci surgical system from Intuitive Surgical is the most commonly used robot for MIS. It allows for 3D visualization, seven degrees of freedom, elimination of tremors, motion scaling, improved dexterity and ergonomic position [8]. The advantages and disadvantages of conventional laparoscopic surgery and robot–assisted surgery are summarized in Table 1.1.

Table 1.1: Advantages and Disadvantages of Conventional Laparoscopic Surgery and Robot–Assisted Surgery [8]

	Conventional Laparoscopic	**Robot–assisted**
Advantages	Well–developed technology	3–D visualization
	Affordable and ubiquitous	Improved dexterity
	Proven efficacy	Seven degrees of freedom
		Elimination of physiologic tremors
		Ability to scale motions
		Tele–surgery
		Ergonomic position
Disadvantages	Loss of touch sensation	Absence of touch sensation
	Loss of 3–D visualization	Very expensive
	Compromised dexterity	High start–up cost
	Limited degrees of motion	Unproven benefit
	Amplification of physiologic tremors	

Even though the da Vinci is the most commonly used surgical robotic system, it is cumbersome, fills a large operating room [20], and is often too costly to justify its use [8], [21], [22]. For example, a case–matched study of 50 patients who underwent robotic–assisted laparoscopic cholecystectomy and 50 who underwent conventional laparoscopic cholecystectomy identified that skin–to–skin operation time and hospital stay were similar. However, at a cost of \$7985, the robotic–assisted laparoscopic cholecystectomy was $\$1,730$ more expensive than conventional laparoscopic cholecystectomy. The main reasons robotic–assisted laparoscopic cholecystectomy is more expensive are the higher purchase, annual maintenance, and consumable costs with the robotic system [21]. Table 1.2 shows the differences between the purchase and maintenance costs of the da Vinci robotic system and conventional laparoscopic equipment.

Table 1.2: Purchase and Maintenance Costs of da Vinci Robotic System and Conventional Laparoscopic Equipment [21]

	Purchase (US$)	**Annual Maintenance (US$)**
da Vinci Robotic System	1,275,000	127,500
Laparoscopic Equipment	72,250	4,250

Approaches that insert a robotic device entirely inside the body are also a focus of current

work on MIS. One tool is an imagining device in the form of a pill that is swallowed and passively moves through the gastrointestinal (GI) track returning thousands of images [23], [24]. Because this pill requires a natural process to advance through the GI track, it cannot be focused to a specific location and the precise locations of the images are unknown. A hybrid locomotion system for a GI track capsule has also been developed and tested. This capsule contains an internal magnet that allows it to be guided in the lower GI tract by an endoscopist using an external magnetic field. Three on–board legs can be actuated by a small permanent magnet direct current motor to dislodge the capsule if it becomes stuck [25]. A real–time wireless camera system is currently being developed to be integrated with this hybrid locomotion system.

Miller *et al.* have described an *in vivo* stereoscopic imaging system as a proof–of–concept design [26]. Based on this concept, a stereoscopic, insertable, remotely controlled camera with digital zoom, picture–in–picture, and marked instrument tracking capability has been design and tested in a porcine model by Fowler *et al.* [27].

Finally, a miniature mobile robot called the Heartlander robot has been developed that can adhere to and move across the surface of the beating heart using vacuum pressure [28]. It has successfully deployed injection needles, pacing leads, and ablation catheters in porcine hearts [29], [30].

1.2.5 Limitations of Improvements to Laparoscopic Surgery

Single–port laparoscopic and natural orifice surgery reduce the number of incisions made in the abdominal wall, which results in less patient trauma. However, single–port laparoscopy using conventional laparoscopic tools further reduces access to the surgical site compared to conventional laparoscopy because only one incision is made versus multiple incisions. Natural orifice surgery may eventually eliminate the need to make any incisions in the abdominal wall; however, current procedures still use an incision for safety and also further reduce access to the surgical site compared to conventional laparoscopy. Robotic systems such as the da Vinci system return lost perception, dexterity, and degrees of freedom to the surgeon; however, this comes at a very high cost and is of limited benefit to the patient compared to

traditional laparoscopic surgery. Finally, *in vivo* devices such as GI tract capsules and the Heartlander robot cannot operate in the open environment of the insufflated abdomen and, therefore, cannot be used for laparoscopic surgery. Due to these limitations with single-port laparoscopy, NOTES, and current robotic systems, another approach to laparoscopic surgery is needed.

1.3 Incorporeal Robotic Assistants

An innovative solution that potentially overcomes the limitations associated with laparoscopic surgery and the drawbacks of large and expensive robotic systems is to insert miniature, incorporeal robotic assistants entirely inside the abdominal cavity through a single laparoscopic port. Because the devices are completely inside the abdominal cavity, they are unconstrained by entry incisions and can be arbitrarily repositioned. A family of fixed–base and mobile robots have been used to enhance visualization of the surgical field, [31], [32], and to obtain tissue samples during a single–port liver biopsy in a porcine model [33]. In addition, camera robots were tested by three NASA astronauts and a surgeon in a submersible habitat 20 m underwater [34]. These tests suggest that incorporeal robots could be used in place of standard laparoscopic equipment without loss of performance, can be deployed effectively in remote and harsh environments, and telementoring can be used to build upon basic skills for more complex procedures [34]. The applications of incorporeal robots are not limited to laparoscopic surgery. An incorporeal robot performed endoscopic transgastric abdominal exploration, demonstrating its ability to be used in natural orifice surgery [35].

The robots mentioned above all relied on tethers for power, control, and data transmission and each was designed for a specific task. A new family of incorporeal robots has been developed that eliminates tethers by using wireless communication and an on–board power supply. Also, the robots have a modular design that allows for rapid development of different payloads without modifying the power and control portion of the robot. The current types of payloads include a biopsy grasper, a stapler and clamp, and physiological sensors that have been tested in *ex vivo* and *in vivo* settings [36]. The tetherless design enables the surgeon to easily relocate the robots inside the abdominal cavity without interference from

one another. In addition, multiple robots used for vision and task assistance can be inserted through a single port. These features alleviate access problems with single–port laparoscopic surgery and reduce patient trauma compared to procedures using multiple entry incisions. Eventually, non–medically trained personal could carry and deploy these types of low–cost and easily transportable robotic devices at the scene of an accident or injury.

Chapter 2

Background on Incorporeal Robots

2.1 Modular Robot Design

The most recent version of the incorporeal robot was designed to be modular and builds on earlier fixed–base and mobile robots [33], [37], [38]. It has two cylindrical bodies that fit together and slide inside two wheels. The body has an outer diameter of 16 mm and is about 100 mm long. Each wheel has an outer diameter of 20 mm and is actuated by a permanent magnet direct current (PMDC) motor that is connected to the wheel through a pair of transmission gears. The robot's movements and actions are controlled by an operator using a remote control that sends wireless commands to a circuit board inside the robot body. Inside one of the cylindrical bodies there is dedicated payload space that allows robots with a variety of tools to be developed by only changing the payload body. Each payload body can be interchanged and connected to the second cylindrical body, the control body, that houses the main control board and battery. This type of interchangeability is the basis for the modular design. A schematic of the robot without an internal payload is shown in Figure 2.1. Overall, the design of the modular robot has three main components: the control body, the payload body, and the wheels [36].

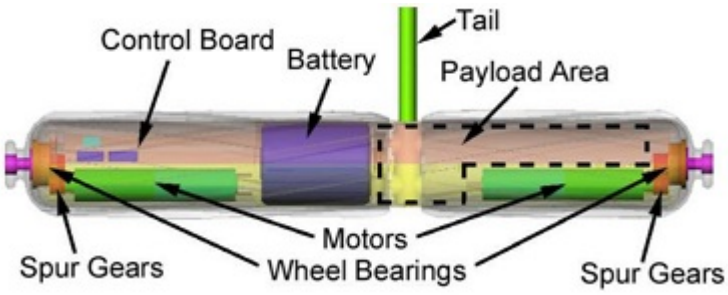

Figure 2.1: Schematic of Base Robot Design [36] (© 2009 IEEE)

2.1.1 Control Body

The control body, shown to the left of the tail in Figure 2.1, is the power plant and brains of the robot. It houses the battery, the control circuit board, and a wheel motor. A lithium organic cell battery (Tadiran TLM–1520MP) with a 185 mAh capacity powers the robot and can last for two hours with all of the motors running continuously. The control circuit board is a custom designed, four–layer, double surface mount, printed circuit board containing a microprocessor, a multichannel motor driver, and an RF transceiver.

The microprocessor (PIC16LF767) is an 8–bit, low–power chip that features 11 10–bit ADC channels, three pulse–width modulation (PWM) outputs, an internal oscillator, and power management functions. These features provide for a small footprint and low power consumption while allowing for the connection to multiple sensors and the independent control of three different motors. The main function of the microprocessor (MCU) is to communicate with peripherals, such as the motor driver, RF transceiver, and various sensors.

Connected to the microprocessor with a three–wire serial interface, the motor driver (Toshiba TB6557FLG) provides up to four voltage controlled and two constant current H–bridge outputs. The current design of the main control board makes three of the voltage controlled H–bridge outputs available. Each wheel motor is connected to one of the outputs with the third available for a payload motor if needed.

Wireless communication to the control board is implemented with a 2.4 GHz ISM band RF transceiver (Nordic nRFA2401) and a single–ended, 50 Ohm chip antenna (LINX ANT–2.45–CHP). In Burst Mode, it is capable of error–checked data rates of up to 1 Mbps. The transceiver also supports 125 receive/transmit channels, which enables simultaneous communication with multiple robots using the same chip without interference between robots [36]. A photograph of each side of the main control board is shown in Figure 2.2.

2.1.2 Payload Body

The cylindrical payload body, shown to the right of the tail in Figure 2.1, is dedicated for different types of payloads. Therefore, it contains a wheel motor and mostly payload space. The robot body is designed in a way that allows the control side to remain almost unchanged

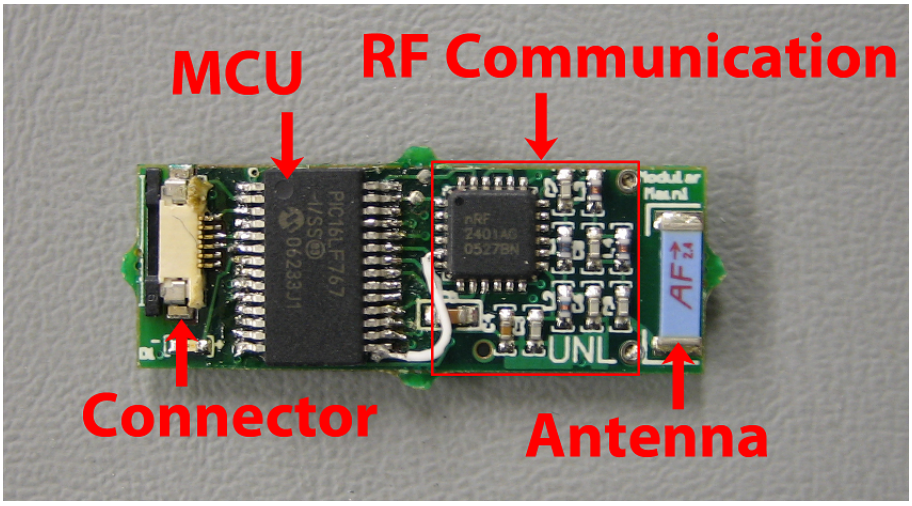

(a)

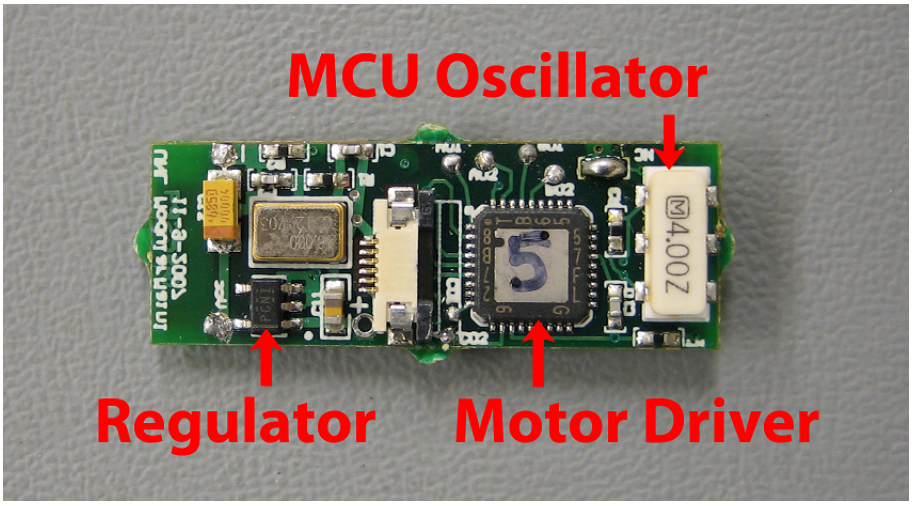

(b)

Figure 2.2: Main Control Board: (a) Front and (b) Back

for different types of payloads.

2.1.3 Wheels

As shown in Figure 2.1, the two body halves of the modular robot are connected at the center and rest inside two wheels. Each wheel is connected to its respective wheel motor through two spur gears and a bearing assembly. The first spur gear is secured to the shaft of the wheel motor and meshes with a second spur gear attached to the bearing assembly. Each wheel is then fastened to the bearing assembly to complete the mechanical connection. The wheel motors are 6–mm diameter, PMDC motors manufactured by MicroMo with an attached 256:1 ratio gearhead. A tail between the gap of the wheels prevents counter–rotation when the robot is driving around. Usually, the tail feature is incorporated into the payload design.

The current wheel design is a result of previous analytical modeling, experimental testing, and finite element analysis. Each wheel is 20 mm in diameter, 0.375 mm thick, and has nine helical grousers. The helical grousers are spaced 7 mm apart with a pitch angle of 10.6°. This configuration allows for smooth motion because at least two grousers are in surface contact at all times [38].

2.2 Current Payloads

Several different payloads currently exist for the modular robot. Each of these payload bodies can function using the same control body by only switching wire connections. The current payloads consist of a sensor package, a biopsy mechanism, and a stapling and clamping mechanism. A robot equipped with a camera also exists but uses a slight variation of the robot body.

2.2.1 Sensor

The modular robot is able to monitor local conditions inside the insufflated abdomen using a sensor payload. This payload is a circuit board containing temperature, pressure, and

relative humidity sensors. It is placed in the payload body and connects to the control body via a six–wire flexible printed circuit (FPC) cable. The sensor data are interpreted by the microprocessor and relayed wirelessly to a receiver module that can display the data on a laptop computer.

2.2.2 Biopsy

Previous designs of the biopsy payload resembled a traditional cable–operated laparoscopic biopsy grasper in that they both use a "grasp and tear" method to obtain a tissue sample. However, this design was inconsistent in obtaining a tissue sample because the robots could not generate enough traction to tear the tissue. The current design of the biopsy mechanism is capable of severing the tissue and then storing the sample in its jaws. As shown in Figure 2.3, a motor in the payload region actuates the biopsy jaws using a linkage assembly for mechanical advantage. A leadscrew is glued to the motor shaft and as it rotates, a leadnut advances, pushing the linkage. The linkage advances a collar to close the biopsy jaws and sever the tissue.

Maximum forces that can be applied by the linkage mechanism were tested to quantify the capabilities of the biopsy payload. When the jaws are completely open, the linkage is fully retracted and can apply a maximum of 7.3 N to the collar. In the fully extended configuration, jaws closed, the linkage can apply a maximum of 13.2 N to the collar [36].

2.2.3 Staple and Clamp

With minor modifications to the biopsy payload, a stapling or clamping robot can be constructed. The same actuation mechanism is used but the sharp biopsy jaws are replaced with rounded and slightly longer ones. These alternate jaws can hold a staple and deliver it to a specific location when the linkage is actuated. When the robot is not carrying a staple, the jaws can be used as a clamping tool. Recent porcine experiments have demonstrated the capability of the clamping payload by closing off a severed blood vessel between its jaws. Figure 2.4 is a photograph showing the biopsy and staple/clamp jaws.

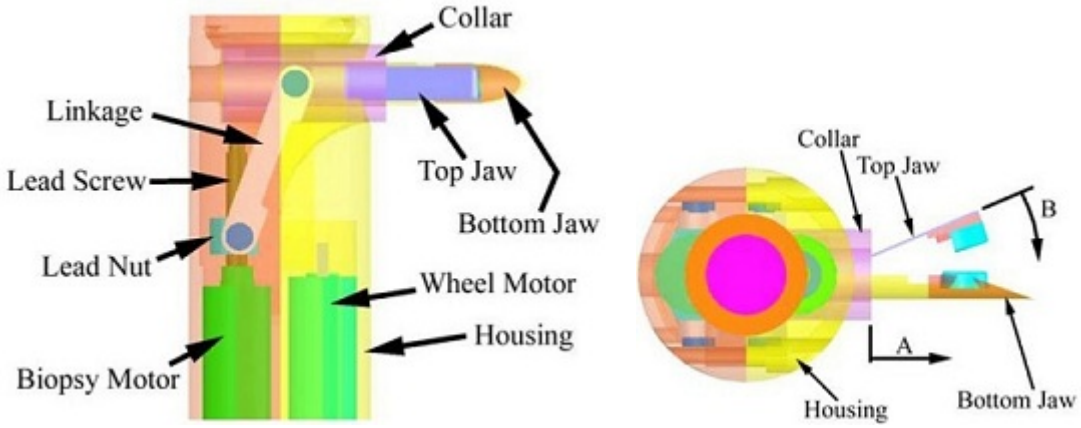

(a) (b)

Figure 2.3: Schematic of Biopsy Payload: (a) Top View and (b) Side View [36] (© 2009 IEEE)

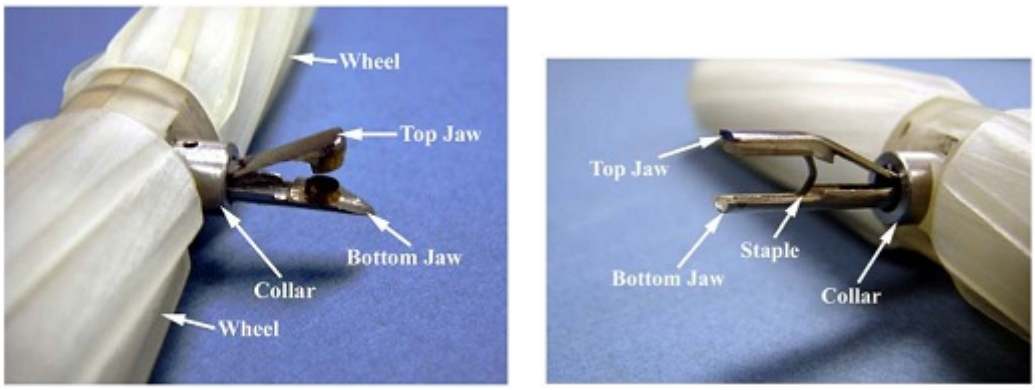

(a) (b)

Figure 2.4: Photographs of (a) Biopsy Jaw and (b) Staple Jaw [36] (© 2009 IEEE)

2.2.4 Ceiling Camera

To provide visual feedback of the operating environment, a modular robot with a camera payload is held at the ceiling of the abdominal wall (Figure 2.5(a)). A magnetic handle placed external to the patient holds the robot to the ceiling of the abdominal wall and allows for a panning motion. This payload has a 6.35–mm digital color CMOS sensor (MT9V125) with 640x480 resolution that can output video data in either NTSC or PAL formats. Three LEDs provide illumination for the camera. An outer housing replaces the wheels with this payload giving the robot the ability to tilt about its cylindrical axis. This is the only robot that has a tether to the exterior of the insufflated abdomen; however, it is only used for transmitting video data because a wireless video transmitter was unavailable at the time. The ceiling pan and tilt robot receives commands wirelessly and receives power from the on–board battery.

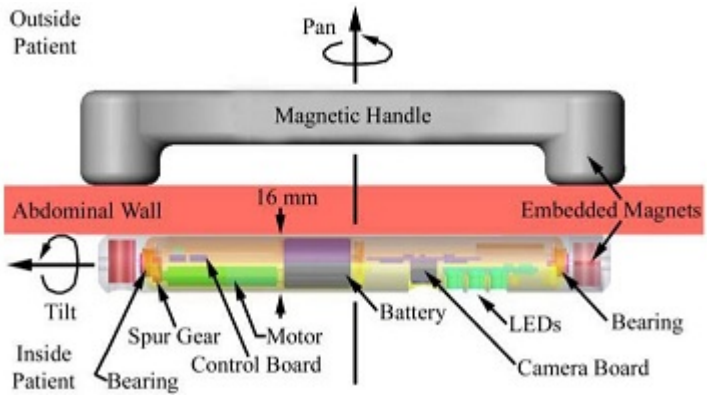

(a)

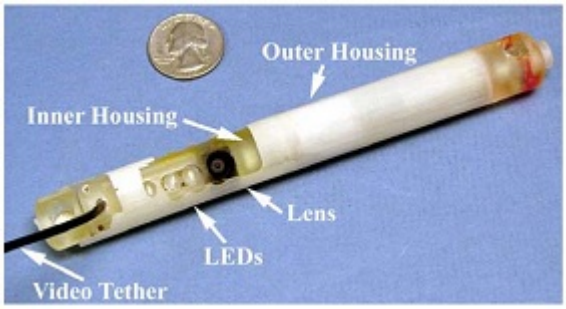

(b)

Figure 2.5: (a) Schematic of Ceiling Camera Robot with Magnetic Handle and (b) Photograph of Robot [36] (© 2009 IEEE)

2.3 Need for Liquid Drug Delivery Payload

The current robot family has several payloads; however, there is not a payload designed to carry and deliver liquid drugs. Two examples of liquid drugs used in conventional surgery and MIS are tissue sealants such as BioGlue and Evicel. These biosurgical compounds have been used as adjuncts or replacements for mechanical means of controlling bleeding or wound closing [39]. Suturing and knot tying used for mechanical fixation, wound closing, and achieving hemostasis require extensive retraining and practice for use in laparoscopic surgery [40]. Therefore, new approaches have been developed such as using staples or titanium tacks in place of sutures in applications such as securing a peritoneal mesh when reinforcing a hernia defect. However, many of these alternatives have been accompanied by nerve damage and chronic pain [41], [42].

Fibrin tissue sealants have the ability to be used as both a hemostat and a tissue adhesive. For example, during a study with 100 laparoscopic partial nephrectomies, fibrin tissue sealant was compared with suture bolstering and it was found that, in certain situations, hemostasis could be achieved with fibrin sealant alone [43]. Another study found the combined use of fibrin glue and Gelfoam alone to be an effective method to achieve hemostasis in the repair of a collecting system injury [44]. An incorporeal robot capable of carrying and delivering a fibrin tissue sealant would combine the advantages of the incorporeal robot family and fibrin tissue sealants.

The main focus of this thesis was on the development and testing of a dual–component, liquid drug delivery payload. There are three main design requirements of this type of payload:

1. A sealed chamber that can separately store two different liquids,
2. A mechanism to dispense the liquids in the chamber, and
3. An ability to mix the two liquids stored in the chamber before they are dispensed (e.g., if fibrin sealant is used).

The work done to address these challenges is presented in Chapters 5–9. In addition, Chapter 10 presents improvements to the design of the main circuit board that address problems seen

repeatedly during previous experiments.

The modular robots have performed successfully in several *in vivo* porcine models. Their ability to maneuver in the abdominal environment has been demonstrated with a single robot and with several robots simultaneously. In addition, each payload has been tested to show it can perform its specific task. However, immediately before every experiment, each modular robot required about 30 minutes of assembly time. This is because there was no method to control the on/off state of the robots except for physically soldering wires to the main control board. This last minute assembly prevents the robots from being tested immediately before an experiment, prevents quick deployment and use, and is an inefficient use of battery power. Therefore, a method for better power management is needed. The work done to address this is presented in Chapter 10 of this thesis.

The modular design of the robots allows for different payload configurations without changing the control body design. In the case of the sensor, biopsy, and staple and clamp payloads, they all shared the same software as well. The software was written for the microprocessor in such a way that it would detect what type of payload was being used and run the appropriate code. This approach was successful but the microprocessor needed to be programmed with the correct software before it was soldered to the main control board. If errors existed in the software or if additional functionality was to be added, a new circuit board had to be used. Therefore, a method is needed to modify the software *a posteriori*. The work done to address this is also presented in Chapter 10 of this thesis.

Chapter 3

Background on Hemostatic Techniques

As with open surgery, uncontrolled bleeding during laparoscopic surgery can cause signification complications. Furthermore, unmanageable bleeding during minimally invasive procedures is the most common indication for reverting to traditional open surgery [45]. One possible application of an incorporeal robot with a liquid drug delivery payload is to assist with hemostasis. Available hemostatic techniques can be grouped into three categories: mechanical, energetic, and tissue sealants.

3.1 Mechanical

The traditional method to treat bleeding is with sutures or mechanical compression. Suture techniques used in open surgery have been adopted and modified for use in laparoscopy [46]. Mechanical compression with cotton gauze is the first method used for hemostasis by many surgeons in open surgery and MIS [47]. In addition to these techniques, hemoclips and staples are both used in MIS to control bleeding from blood vessels [46], [47].

3.2 Energetic

Similar to hemoclips and staples, energetic methods of achieving hemostasis are primarily used for dissection, adhesiolysis, and division of vascular structures [47]. Instruments used in these methods include an electrocautery, an ultrasonic or harmonic scalpel, an argon beam coagulator, and a laser. A bipolar electrocautery allows for simultaneous dissection and coagulation of tissue. Electrical current flows between the jaws of grasping instruments that thermally severs the tissue. Damage to surrounding tissue is minimized when using

a biopolar device versus a monopolar device [46]. An argon beam coagulator combines an inert gas jet with an electrocautery device. The argon gas jet clears blood and debris from the site allowing for more effective hemostasis [48]. An ultrasonic or harmonic scalpel uses high frequency ultrasound to cut and coagulate tissue. At a frequency of 25 kHz, tissue dissection occurs and at frequencies greater than 55 kHz, coagulation occurs as well [46]. Lasers provide the ability to simultaneously dissect and coagulate tissue; however, their application causes significant tissue vaporisation and spreading of liquid [46]. The Holmium laser has been used in several procedures; however, clinical data is very limited and lasers remain mostly experimental in laparoscopy [46], [49].

3.3 Tissue Sealants

Fibrin glues are the most common tissue sealants used in laparoscopy [46]. Fibrin glue is a two–component mixture of thrombin and fibrinogen that combine to form a solid fibrin matrix [50]. The two individual components make up the last stages of the clotting cascade and have hemostatic and adhesive properties resulting in improved hemostasis when used to control bleeding compared to other tissue sealants such as gelatin matrix. Currently, fibrin tissue sealants are administered through a long needle with a dual–lumen adapter. The components are stored separately until immediately before use and are mixed as they pass through the dual–lumen adapter [46], [47]. Also, the components are all biodegradable and disappear from the body within 3 to 4 weeks [50].

Gelatin matrix is a bovine derived, two–component tissue sealant consisting of thrombin and gelatin matrix granula. After the components are mixed in a syringe before application, the matrix can be used for up to two hours [49]. Also, after application, it can be compressed with a surgical sponge without sticking and will only cause coagulation where fibrinogen is present at the bleeding location [50].

Oxidized regenerated methylcellulose is a tissue fleece (i.e., a mesh scaffold) that can be applied on surfaces with minimal bleeding [46], [49]. The fleece is sutured or secured with fibrin glue to the site and applies local compression along with supporting local hemostasis of the cellulose tissue [46].

3.4 Application to Incorporeal Robots

Fibrin sealants have advantages over mechanical and energetic methods of hemostasis. As discussed in Section 2.3, there are several problems associated with mechanical methods of hemostasis in laparoscopic surgery. For example, suturing requires extensive retraining, and nerve damage has accompanied the use of staples and tacks. Energetic means of hemostasis require a relatively large energy source, as with electrocautery tools and harmonic scalpels, and can damage surrounding tissue. Studies have shown that hemostasis can be achieved with fibrin sealant alone, with fibrin sealant as a suture bolster, or with fibrin sealant and another tissue sealant [43], [44].

An incorporeal robot capable of carrying and delivering a fibrin tissue sealant combines the advantages of the incorporeal robot family and fibrin tissue sealants. The two components of a fibrin sealant need to be stored separately inside the robot and then mixed before it is dispensed. Therefore, in addition to a method for storing and dispensing liquids, a method for mixing liquids needs to be incorporated into the payload design. As discussed in Section 2.3, the main focus of this thesis was the development and testing of a payload that can store, dispense, and mix liquids. A method for mixing liquids is discussed in Chapter 4. The methods developed for successfully storing and dispensing liquids are discussed in Chapter 5, and the testing of mixing performance is discussed in Chapters 6 and 7.

Chapter 4

Background on Static Mixing Devices

4.1 Static Mixers

In passive mixing, liquids flow over stationary fins or blades that disrupt the flow and induce mixing. Devices used to passively mix liquids are called static or motionless mixers and have become standard in process industries. Advantages of static mixers, compared to active mixers, include their small space requirement, low equipment cost, no power requirement except for pump, lack of moving parts, and good mixing at low shear rates [51].

Two common static mixers are the Kenics KM helical mixer and the SMX mixer, shown in Figure 4.1. The helical mixer consists of alternating right–hand and left–hand 180° twisted elements and the SMX mixer has multiple sections of blades arranged in an "X" pattern with each section rotated 90°. The Kenics KM helical mixer is designed for both laminar and turbulent flow regimes with liquid–liquid or gas–liquid mixtures [52]. The SMX mixer is designed for highly viscous, laminar flows [53].

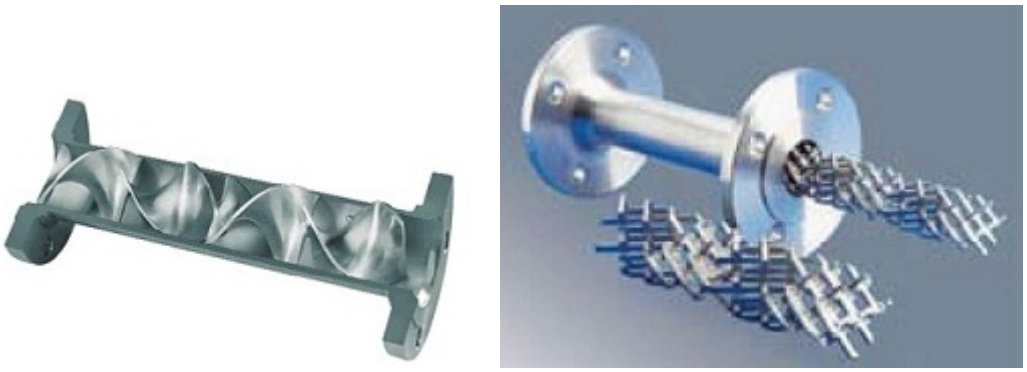

(a) (b)

Figure 4.1: Common Static Mixers: (a) Kenics KM Mixer from Chemineer [52] (© 2010 Chemineer) and (b) SMX Mixer from Sulzer Chemtech [53] (© 2010 Sulzer Chemtech Ltd)

4.2 Evaluation of Static Mixers

Static mixers are usually evaluated based on the additional pressure drop the mixing elements cause relative to an empty pipe and the degree of mixing achieved [51], [54]. The additional pressure drop is a non–dimensional number called the Z–factor and is defined by Equation 4.1,

$$Z = \frac{\text{Pressure drop in a pipe with static mixer}}{\text{Pressure drop in a pipe without static mixer}}. \tag{4.1}$$

The degree of mixing is usually determined using statistical methods. A common parameter used is the coefficient of variation (COV) [51], [55], which represents the degree of homogeneity at a given time and tells the relative deviations from the mean. To describe the COV in more detail, consider a two–component mixture with the concentration of component 1 and component 2 denoted by c_1 and c_2, respectively. The mean concentration $\bar{c}_1$ over N sampling regions is given by Equation 4.2, where $c_{1,i}$ denotes the concentration at sampling region i,

$$\bar{c}_1 = \frac{1}{N}\sum_{i=1}^{N} c_{1,i}. \tag{4.2}$$

The standard deviation of concentration s_1 is given by Equation 4.3,

$$s_1 = \sqrt{\frac{1}{N-1}\sum_{i=1}^{N}(c_{1,i} - \bar{c}_1)^2}, \tag{4.3}$$

and finally the coefficient of variation is give by Equation 4.4,

$$\text{COV} = \frac{s_1}{\bar{c}_1}. \tag{4.4}$$

The COV ranges from zero to infinity, with an ideally homogeneous mixture having a value of zero. However, this parameter does not indicate a threshold that should be achieved during the mixing process. For example, a COV value of 0.05 is used as a rule–of–thumb to estimate fully mixed conditions, but for different mixing processes a range of values are used [56].

Another method to evaluate mixing is based on the concept of intensity of segregation from Danckwerts [57]. Again, consider a two–component mixture with the concentration of component 1 and component 2 denoted by c_1 and c_2, respectively. The intensity of segregation I is defined by Equation 4.5,

$$I = \frac{\sigma_{c_1}^2}{\bar{c_1}(1-\bar{c_1})}, \tag{4.5}$$

where $\sigma_{c_1}^2$ is the variance of the concentration and $\bar{c_1}$ is the mean concentration of component 1. The denominator in Equation 4.5 can be shown to be equal to a maximum variance $\sigma_{c_1,max}^2 = \bar{c_1}(1-\bar{c_1})$ [58] that is computed by considering the mixture components separately [59], [60]. This leads to a segregation index that is normalized by a maximum value and is given by Equation 4.6,

$$I_s = \frac{\sigma_{c_1}^2}{\sigma_{c_1,max}^2}. \tag{4.6}$$

A typical example for measuring the intensity of mixing is given by Equation 4.7,

$$I_M = 1 - \sqrt{I_s} = 1 - \frac{\sigma_{c_1}}{\sigma_{c_1,max}}, \tag{4.7}$$

and because I_s is normalized, I_M takes a value of 0 for completely segregated mixtures and a value of 1 for the homogeneously mixed case [59]. This normalization allows for a more intuitive interpretation of the mixedness of two liquids compared to the COV, which ranges from zero to infinity.

4.3 Analysis Methods of Static Mixers

Several physical methods have been used to measure the concentration values needed to evaluate static mixers. Pahl *et al.* [54] evaluated several static mixers by using a sugar syrup (viscosity of $\eta = 6$ Pa·s) with 10% of the syrup made using NaOH. Nonuniform distribution of NaOH led to conductivity differences in the syrup and were measured by transversing an electrode at the mixer exit. Of the mixers tested, the Sulzer SMX required the shortest length of hose to produce homogenization. Also, for laminar flow, the Kenics

helicial mixer was calculated to have the smallest Z–factor of the group.

Another method used to study the performance of static mixers is Planar Laser Induced Fluorescence (PLIF) [61], [62]. In PLIF, a fluorescent dye is injected upstream of the static mixer and the dye concentration is measured at a downstream plane. To measure the downstream concentration, a laser sheet illuminates a transparent section of pipe which fluoresces the dye in that planar section. The intensity of fluorescence is related to the dye concentration and images of the dye fluorescing are captured with a camera. The degree of mixing can be calculated through analysis of the captured images.

A third method for measuring the degree of mixing is using two different color liquids and analyzing the resulting color distribution in the mixture from images captured with a camera. This is a common technique for evaluating micromixers. For example, water used as the working fluid enters the experimental setup through two separate inlets. Water entering through the first inlet is dyed black and water entering through the second inlet is undyed. A camera is positioned above the mixer and images are captured at a transparent section that is illuminated from beneath with a diffuse, even light source. The color intensity in the image can then be analyzed to give a quantitative analysis of mixing [63], [64].

Detailed analysis on static mixers using physical experiments can be difficult due to complex geometry of mixers and the extensive setup required for non–intrusive measurement techniques. Their complicated geometry also makes detailed, analytical analysis almost impossible. Therefore, numerical analysis called computation fluid dynamics (CFD) has become a useful tool in studying static mixers. Usually, commercial CFD packages (e.g., Fluent) are used for the numerical analysis. Two methods for evaluating mixing in CFD simulations are particle tracking with a single working fluid and species concentration of two fluids. CFD simulation results for static mixers have been validated by comparisons to experimental data. For example, Zalc *et al.* [65] used a particle tracking method to rate mixing in CFD simulations of a SMX mixer and found good agreement with previously published experimental data. In another example, Lee and Kwon [63] found good agreement of mixing performance between a two–fluid species concentration CFD simulation and a color dilution experiment for a micromixer.

4.4 Application to Incorporeal Robots

Due to the small size of the static mixer used with the liquid drug delivery robot and the relative ease of experimental setup, a color dilution method was used to evaluate mixing during the physical experiments presented in Chapter 7 of this thesis. In addition, these experimental results validated species concentration CFD simulations. Once validated, simulation was used to explore static mixing designs more quickly than could be done in physical experiments. Details of the numerical simulations are described in Chapter 6.

The design of a liquid drug delivery payload could incorporate a static mixer to mix liquids stored inside the payload body. Preliminary static mixer designs are shown in Section 6.1 that incorporate the mixer into a hose extending from the robot body.

Chapter 5

Payload Concept and Verification

5.1 Concept

Based on the three general design requirements for having a liquid drug delivery payload:

1. A sealed chamber that can separately store two different liquids,
2. A mechanism to dispense the liquids in the chamber, and
3. An ability to mix the two liquids stored in the chamber before they are dispensed (if fibrin sealant is used),

a prototype concept was designed. A region in the payload body between the wheel motor and connection to the control body was hollowed out to create the liquid reservoir. To seal the reservoir from the rest of the payload body, a syringe–like plunger was designed. A PMDC motor in the payload region is used to actuate the plunger using a leadscrew and leadnut assembly to expel liquid from the reservoir through small exit ports. The plunger is split into two semi–circular heads to allow it to slide over a center divider. The center divider bisects the reservoir and serves multiple purposes. First, it allows for separate storage of two different liquids. The split design also prevents rotation of the plunger and constrains its motion to translation. Finally, a slot in the center divider provides space to feed through electrical wires that connect to the wheel and payload motors. From the resulting concept, a 3D computer model was constructed, shown in Figure 5.1.

The payload body containing the bisected reservoir and the payload motor is a single piece that has two charging ports (0.35 mm in diameter) that allow each reservoir compartment to be filled separately using a 30–gage needle and syringe after the robot is fully assembled.

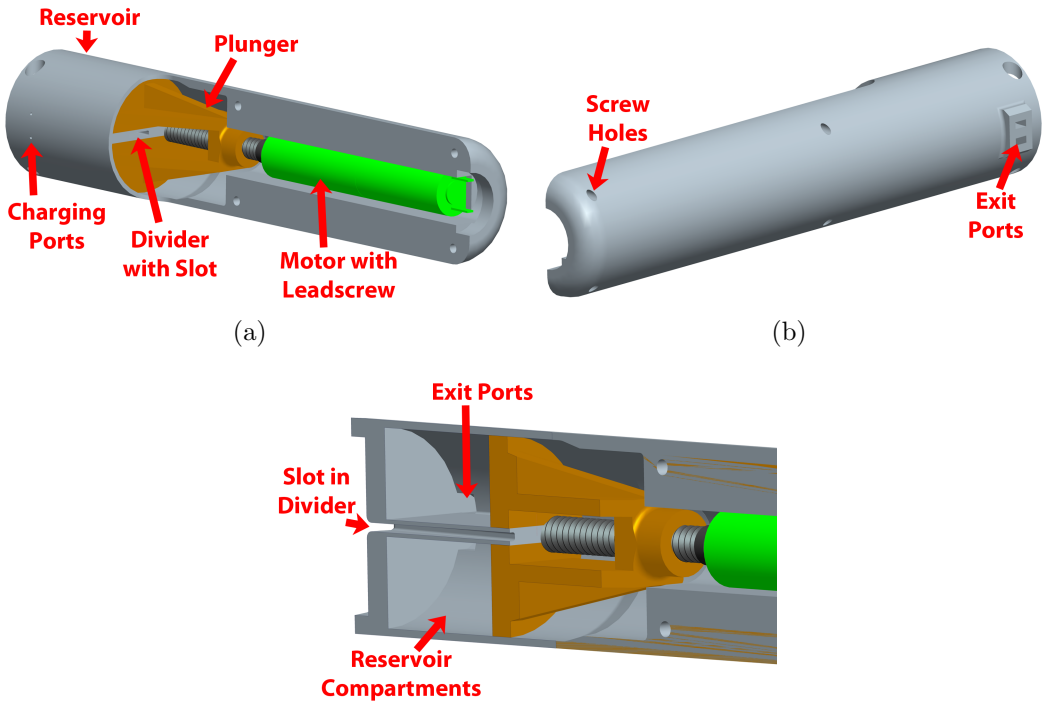

Figure 5.1: (a),(b) Overview and (c) Cut–away View of Liquid Delivery Payload Concept

Exit ports for the reservoir can be seen in Figure 5.1(b). A hose extending from these exit ports helps deliver the liquid to a specific location. The hose can either be empty or have internal fins to replicate a static mixer. The maximum usable volume of liquid is 1.7 ml; however, this amount can vary slightly depending on the configuration of the hose used. This amount of liquid is similar in volume to a standard 2.0 ml package of the fibrin sealant Evicel [66]. In addition, the small size of the hose allows for the administration of the appropriate dosage in the form of 0.1–0.2 ml drops [66] to produce a thin, even layer.

The syringe–like plunger and split reservoir concept described above was experimentally tested before a complete prototype was built to verify that the payload motor could produce an adequate push force to actuate the plunger, and to identify a plunger design that would provide a leak–free seal.

5.2 Dispensing Mechanism Testing

To actuate the plunger successfully, the payload motor needs to be powerful enough to overcome resistance from the fluid–wall shear stress, the decrease in cross–sectional area from reservoir entrance to exit, the friction between the plunger and reservoir walls, and losses in the leadscrew and leadnut mechanism. The leadscrew and leadnut mechanism was assumed to be part of the motor and, therefore, performance losses from it were included into the performance of the motor.

5.2.1 Maximum Motor Push Force

The maximum push force that the payload motor could generate was measured using the experimental setup shown in Figure 5.2. A 4–40 threaded stainless steel screw was cut to create a leadscrew and mounted onto the motor shaft. The motor was secured in a stand fabricated with rapid prototyping techniques using FullCure 720 Transparent material on an Eden 350 3D printer. A threaded nylon stand–off was attached to each side of a load cell (ELFM–T2E–25L) with one stand–off screwed onto the leadscrew and the second stand–off allowed to slide through a mounting piece that was also rapid prototyped. Fastened to the other end of the second stand–off, another stainless steel screw pressed against a 4–mm thick aluminum plate that was held in place using a C–clamp. The motor was supplied with three different voltage levels (3.0 V, 3.8 V, and 4.5 V) using a power supply, and the output of the load cell was recorded at motor stall for each voltage level. These three levels span the range the on–board battery can supply during operation. At each voltage level, three trials were performed and the outputs were averaged to give a maximum push force from the motor and leadscrew mechanism. The results of this test are shown in Figure 5.3.

5.2.2 Major and Minor Head Loss

The resistance generated from the fluid–wall shear stress and the decrease in cross–sectional area from reservoir entrance to exit, referred to as major and minor head loss, respectively, was estimated using conservation of mass and energy. A simplified schematic of the reservoir

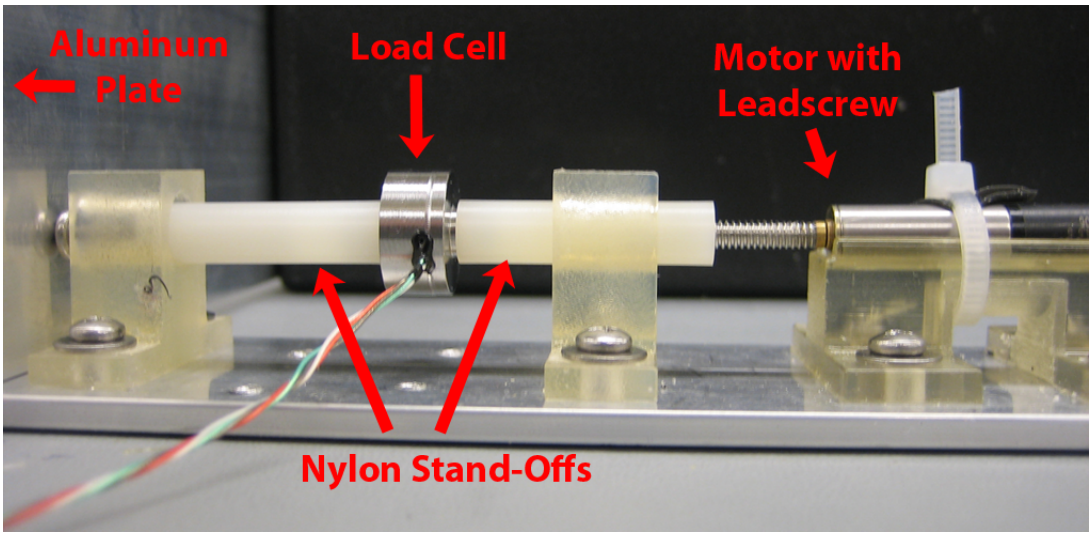

Figure 5.2: Setup for Measuring the Maximum Push Force of the Payload Motor

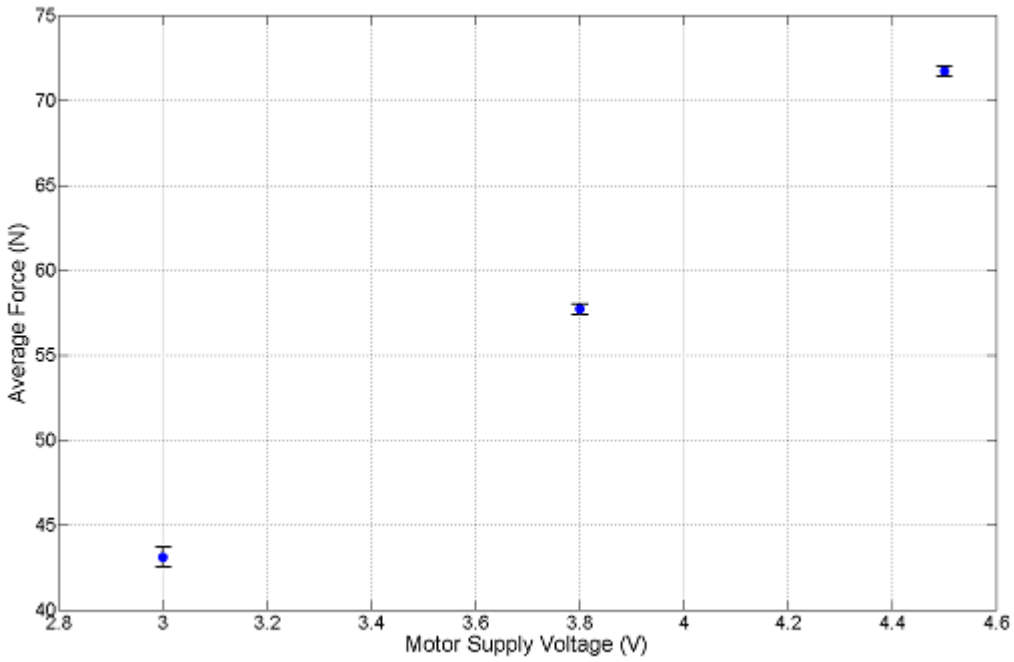

Figure 5.3: Maximum Push Force Test Results of 615 C 4.5 S Motor with 256:1 Gearhead

used for these calculations is shown in Figure 5.4. Conservation of mass requires the mass

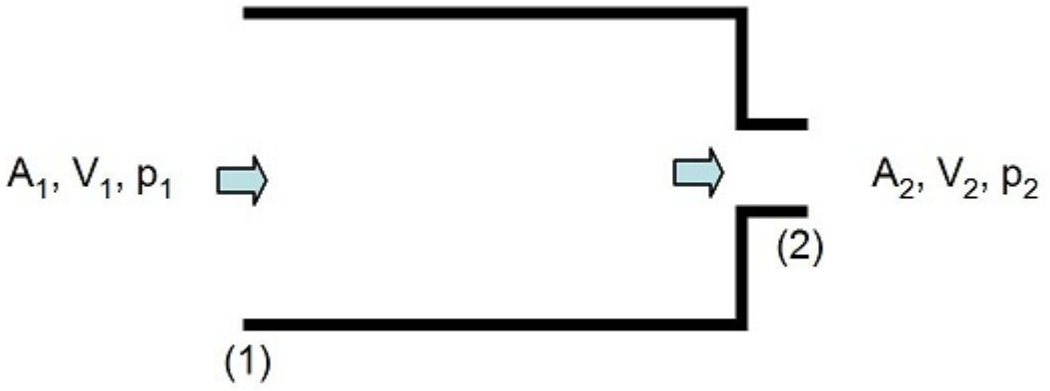

Figure 5.4: Simplified Schematic of Reservoir

flow rate $\dot{m}_1$ through the cross–sectional area of the reservoir entrance A_1 to equal the mass flow rate $\dot{m}_2$ through the cross–sectional area of the reservoir exit A_2. The flow is assumed to be uniform at sections (1) and (2), at constant pressure along section (1), and incompressible, which results in Equation 5.3 for the exit velocity V_2 based on the entrance velocity V_1 and ratio of cross–sectional areas:

$$\dot{m}_1 = \dot{m}_2 \tag{5.1}$$

$$\rho_1 A_1 V_1 = \rho_2 A_2 V_2 \tag{5.2}$$

$$V_2 = V_1 \frac{A_1}{A_2}. \tag{5.3}$$

This expression for V_2 was used with the energy equation (5.4) to obtain the pressure drop $\Delta p = p_1 - p_2$ across the simplified reservoir

$$\frac{p_1}{\rho g} + \frac{V_1^2}{2g} = \frac{p_2}{\rho g} + \frac{V_2^2}{2g} + h_L, \tag{5.4}$$

where $h_L = h_{L,major} + h_{L,minor}$ accounts for the major and minor head loss. For a constant diameter, horizontal, and fully developed flow, the major head loss can be expressed as

$$h_{L,major} = f \frac{l}{D} \frac{V_1^2}{2g}, \tag{5.5}$$

where f is the friction factor, l is the reservoir length, and D is the reservoir diameter. For fully developed laminar flow, the friction factor is only a function of the Reynolds number and expressed as $f = 64/\mathrm{Re}$. The Reynolds number inside the reservoir is defined as

$$\mathrm{Re} = \frac{\rho V_1 D}{\mu}, \tag{5.6}$$

where μ is the dynamic viscosity of the fluid. The Reynolds number inside the reservoir was calculated to be 9 for water at 20°C, indicating laminar flow. The minor loss for a sudden contraction in diameter is shown in Equation 5.7,

$$h_{L,minor} = K_L \frac{V_2^2}{2g}, \tag{5.7}$$

where K_L is a loss coefficient that is a function of the area ratio [67]. Substituting Equations 5.3, 5.5, and 5.7 into the energy equation and solving for $\Delta p = p_1 - p_2$ results in Equation 5.8 for the pressure drop across the reservoir.

$$\Delta p = V_1^2 \frac{\rho}{2} \left[\left(\frac{A_1}{A_2} \right)^2 (K_L + 1) + f \frac{l}{D} - 1 \right] \tag{5.8}$$

The entrance velocity $V_1 = 0.6$ mm/s was estimated by measuring the velocity of the plunger when attached to the leadscrew. The area ratio was estimated by using dimensions from the 3D concept model, and water was used as the working fluid ($\mu = 1.003 \cdot 10^{-3}$ Pa·s and $\rho = 998.2$ kg/m^2). The resulting estimated pressure drop of $\Delta p = 0.24$ Pa was then multiplied by the entrance cross–sectional area to give the force required to push water through the reservoir. A force of $3.8 \cdot 10^{-5}$ N was calculated which is very small compared to the 43 N motor stall push force produced at the minimum supply voltage (3.0 V). Repeating this calculation using glycerin as the working fluid ($\mu = 0.799$ Pa·s and $\rho = 1259.9$ kg/m^2), which is approximately 800 times as viscous as water, results in a required push force of $1.7 \cdot 10^{-4}$ N which is also very small compared to the motor capabilities. Therefore, the contribution of the loss generated by the fluid and geometry was neglected and the resistance seen by the leadscrew mechanism must be mostly generated by the friction between the

plunger and reservoir walls.

5.3 Plunger Seal and Actuation Testing

The resistance from the fluid was estimated to be negligible so it was assumed the resistance seen by the motor and leadscrew mechanism must mostly be generated by friction between the plunger and reservoir walls. Depending on the type of seal between the plunger and reservoir walls, this resistance could be very small where it would not affect the motion of the plunger or it could be very large where it would prevent the plunger from translating. A seal that generates almost no friction usually has little interaction with the walls and, therefore, has a high potential to leak. On the other hand, a leak–free seal usually has high interaction with the walls, but if this interaction is too intense, the plunger would be immovable by the payload motor. This means that a plunger design must be found that allows for a leak–free seal but is easily translated by the payload motor.

5.3.1 Experimental Setup

To find a seal that meets this balance, an experiment was constructed and three different plunger designs were tested. This experimental setup builds on the one used for the motor push force test (Figure 5.2) but instead of pushing against a stationary plate, a plunger translated inside a replica of the fluid reservoir. A photograph of the experimental setup is shown in Figure 5.5 and the three different plunger designs are shown in Figure 5.6.

The replica reservoir, plunger design 1, cylindrical connectors, motor stand, and supports were all fabricated using rapid prototyping techniques from FullCure 720 Transparent material using an Eden 350 3D printer. Plunger designs 2 and 3 were also made from FullCure 720 but use a rubber–like material glued around the plunger head to form a seal between the plunger and reservoir walls. Also made on the Eden 350 3D printer, this material is called Tango Black and is shown in black in Figure 5.6. Plunger design 1 was sized slightly smaller than the reservoir so that it would slide but still have wall contact. The rubber–like seal in plunger designs 2 and 3 were sized slightly larger than the reservoir so that it would press

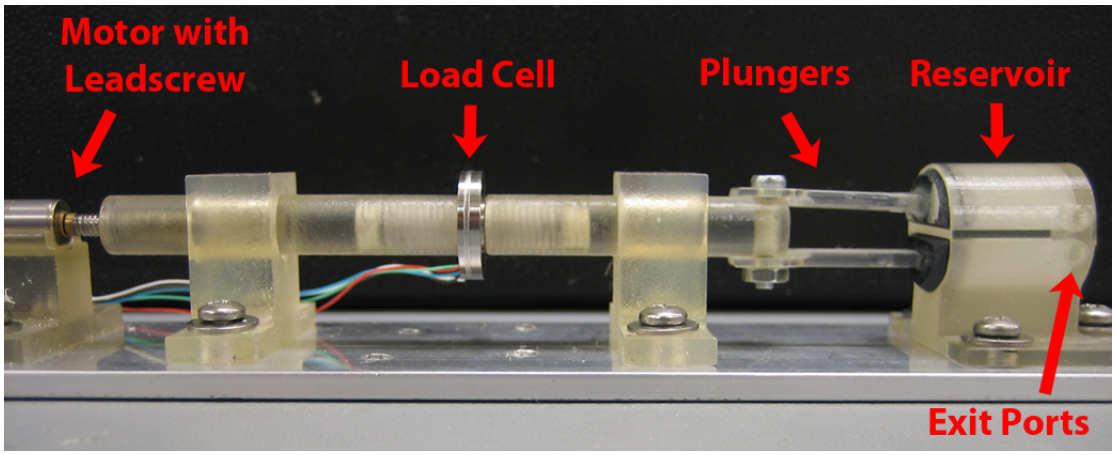

Figure 5.5: Seal Design Experimental Setup

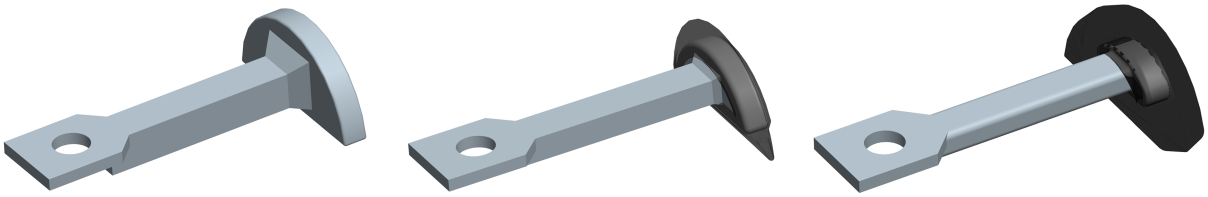

(a) (b) (c)

Figure 5.6: (a) Plunger Design 1, (b) Plunger Design 2, (c) Plunger Design 3

against the reservoir walls.

Each plunger design was attached to the second connector with a screw and translated along reservoir. The reservoir was filled with water during each test to observe the amount of leakage with each design. The motor was supplied with the minimum voltage seen during operation, 3.0 V. To measure the required push force, the output of the load cell was measured with a multimeter sampling at 6 Hz and recorded using a laptop computer that was connected to the multimeter.

5.3.2 Experimental Results

Plunger design 1 leaked significantly during testing and, therefore, was not considered as a design choice. At the start of testing plunger design 2, the seal material around the plunger head immediately ripped and, therefore, was also not considered as a possibility. Plunger design 3 provided a leak–free seal and did not fail. The required push force for this seal along with the push force at motor stall are plotted in Figure 5.7. These test results show that plunger design 3 provided the balance needed to have a leak–free seal and still be movable by the motor and leadscrew mechanism. Due to the margin between the required push force and maximum push force at the minimum voltage supply shown in Figure 5.7, a smaller ratio gearhead could be used and still provide adequate push force. Because a smaller gear ratio shortens the length of the gearhead, and the length of the payload body is determined by the length of the reservoir and leadscrew motor, decreasing the length of the gearhead will decrease the length of the payload body.

5.4 Final Plunger Design

The final plunger design used for subsequent work is a slight modification of plunger design 3 to make assembly easier. Instead of a rectangular extrusion as shown in Figure 5.6(c), the plunger head was modified to have a flat backing surface and a small boss that extends into the rubber seal. A 3D model of the final design is shown in Figure 5.8 and photographs of the final design are show in Figure 5.9. The final design of the plunger head and payload

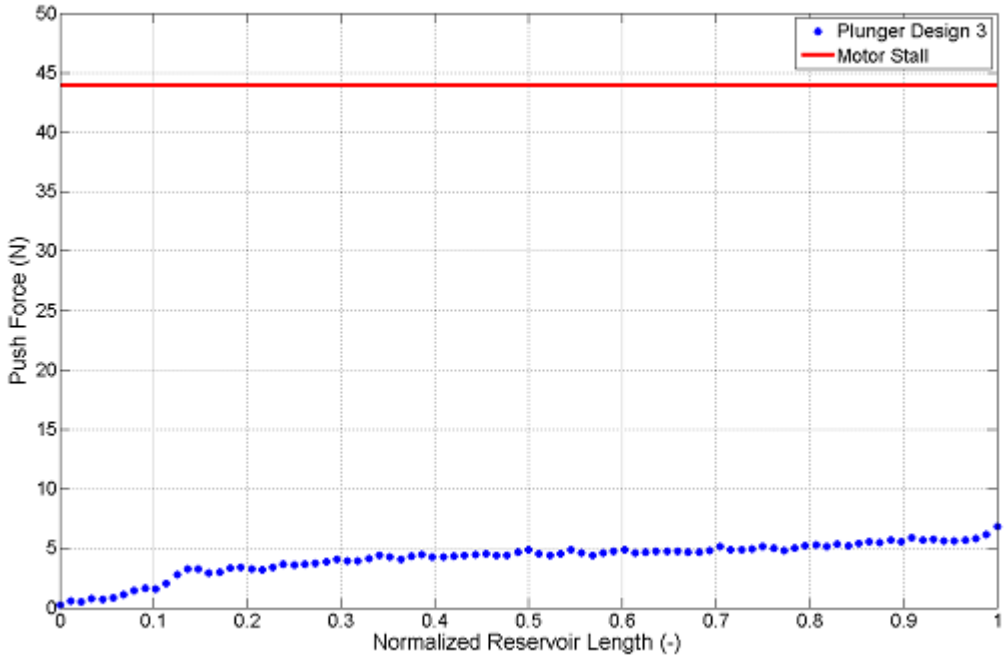

Figure 5.7: Required Push Force of Plunger Design 3 and Push Force at Motor Stall with a Motor Supply of 3.0 V

body were built from WaterClear Ultra 10122 material using stereolithography (SLA) rapid prototyping techniques.

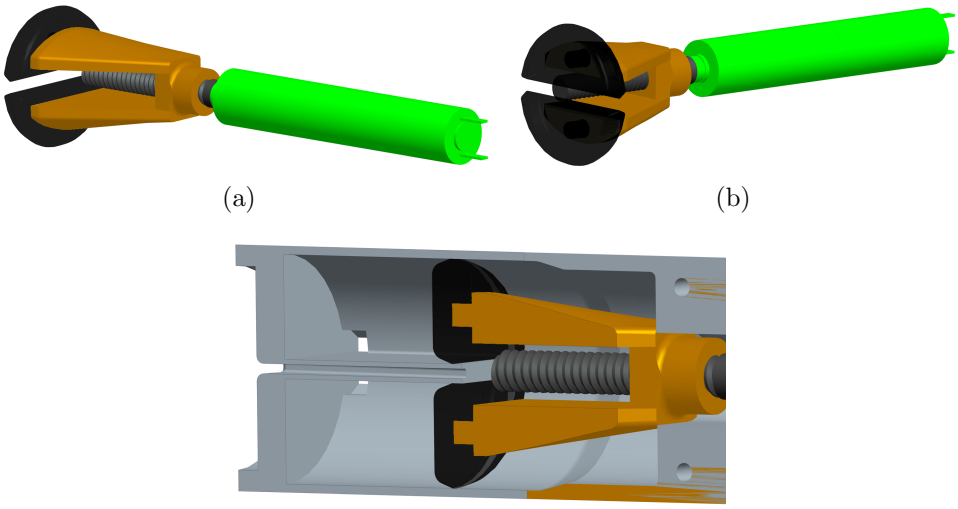

(a) (b)

(c)

Figure 5.8: (a), (b) Final Plunger Design with Motor, (c) Cross–sectional View of Final Plunger Design Inside Reservoir

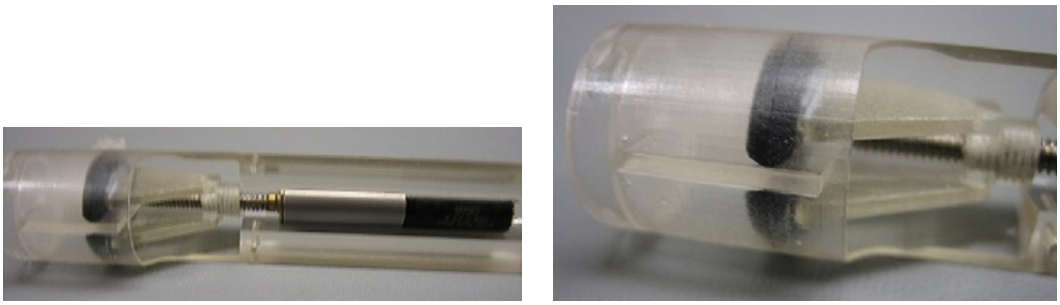

(a) (b)

Figure 5.9: (a) and (b) Photographs of Payload Body with Final Plunger Design and Motor

Chapter 6

Numerical Investigation

The fluid delivery payload needs a hose–like attachment at the reservoir exit ports to deliver the liquid to a specific location and to provide a mixing mechanism. The hose interior can have different configurations depending on the desired application. For example, when using a single type of liquid, the hose interior can be empty. If two different liquids are used that need to be mixed, such as a fibrin sealant, the hose can be made with internal fins to represent a static mixer. The small size of the hose and capabilities of available rapid prototyping techniques only allowed for simplified versions of commercial static mixers to be incorporated into the hose. Prior to fabricating and testing different hose designs, CFD simulations were performed using ANSYS Fluent 12.1 to predict the performance of the different designs. This Chapter discusses simulations that were performed prior to testing and Chapter 7 discusses experimental verification of the simulations.

6.1 Hose Designs

Three different hose designs were compared in preliminary simulations: a plain hose, a cross–blade hose based on the SMX mixer from Sulzer Chemtech, and a hose with triangular tabs based on the HEV mixer from Chemineer. The HEV style hose has triangular tabs extruding from the walls and the SMX style hose has four sections of blades arranged in an "X" pattern. Each section along the length of the hose is rotated 90° relative to the previous section. These hose designs were chosen because they were possible to build with SLA rapid prototyping techniques and they were expected to produce different degrees of mixing relative to each other. The plain hose was expected to produce no mixing, the HEV style hose was expected to produce low to moderate mixing, and the SMX style hose was

expected to produce moderate to high mixing. As discussed in Chapter 4, the Sulzer SMX required the shortest length of hose to produce homogenization. Each hose design with a side wall cut–away and dimensions is shown in Figure 6.1.

6.2 Simulation Setup

For each hose design, the reservoir and the size of exit ports do not change. Therefore, to reduce calculations, only the flow through hose was simulated. The continuity and Navier–Stokes equations were solved numerically to obtain the flow field through the different hoses. For incompressible fluids, the continuity equation reduces to

$$\nabla \cdot \mathbf{V} = 0, \tag{6.1}$$

where ∇ represents the gradient operator and $\mathbf{V}$ is the velocity vector. For steady flow, the Navier–Stokes equation reduces to

$$\mathbf{V} \cdot \nabla \mathbf{V} = -\frac{\nabla p}{\rho} + \mathbf{g} + \nu \nabla^2 \mathbf{V}, \tag{6.2}$$

where p is the fluid pressure, ρ is the fluid density, $\mathbf{g}$ is the acceleration vector due to gravity, and ν is the kinematic viscosity of the fluid. The mixing in the fluid can be expressed by the convective–diffusion equation,

$$(\mathbf{V} \cdot \nabla) c = D \nabla^2 c, \tag{6.3}$$

where c is the mass fraction and D is the binary diffusion coefficient. To solve these equations numerically, the fluid region inside each hose was modeled and meshed with finite volume elements using a target edge length of 0.1 mm. The automatic mesh tool in ANSYS 12.1 was used to apply a structured, hexagonal mesh wherever possible and tetrahedral elements where hexagonal ones were not practical or possible. For example, the plain hose could be meshed with only hexagonal elements but the SMX style hose contains some tetrahedral elements due to the complicated geometry. Figure 6.2 shows an overview of the SMX style

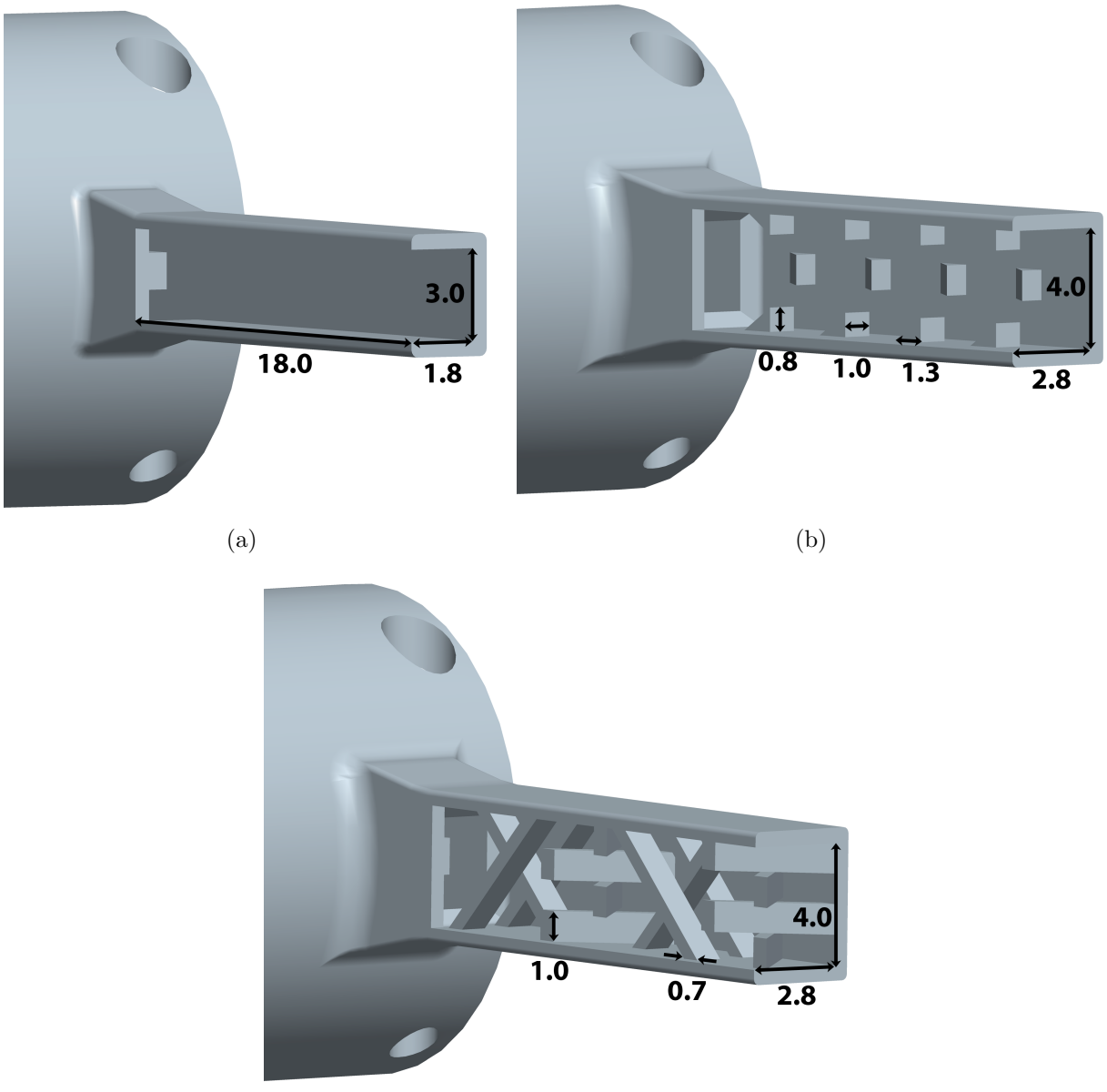

(a) (b)

(c)

Figure 6.1: Cut–away View of Hose Designs (All Dimensions in Millimeters): (a) Plain Hose, (b) HEV Style Hose, (c) SMX Style Hose

geometry and an enlarged view showing the mesh details.

The flow through the hose was modeled as laminar with two separate inlets and one outlet using constant velocity and outflow boundary conditions, respectively. A laminar model was chosen because the Reynolds number was estimated to be 70 for water in the plain hose. Liquid flows from the reservoir compartments, through the hose, and then exits the robot. Therefore, each inlet of the hose shown in Figure 6.2(a) represented the exit port of each reservoir compartment. The hose inlet flow velocity of $V_1 = 17.6$ mm/s was calculated using the simplified reservoir schematic in Figure 5.4, Equation 5.3, and the estimated reservoir entrance velocity of V_2 =0.6 mm/s. Gravity was set in the negative Z–direction (Figure 6.2(a)). Water was used as both working fluids using a no–slip boundary condition with the walls. To evaluate mixing in the hose, fluid entering through each inlet was defined separately using the Species Transport model in Fluent which allows for the output of the mass fraction of each fluid in each element. The mass fraction data were used as the concentration values necessary to calculate a mixing efficiency according to Equation 4.7. This metric was used because it rated mixing on a scale from 0% to 100%. A constant diffusion coefficient was assumed and set to 10^{-9} m^2/s, which is a typical value for the interdiffusion coefficient of water. To reduce unphysical numerical diffusion, the high order discretization scheme Third–Order MUSCL was used.

6.3 Preliminary Simulation Results

Each of the three hose designs were simulated and rated based on how mixed the two fluids were at the outlet of the hose using Equation 4.7. The maximum standard deviation $\sigma_{max} = 0.5$ was determined by considering the completely unmixed case where half of the elements have a mass fraction of 1 and half of the elements have a mass fraction of 0. The standard deviation σ was calculated for each hose by measuring the mass fraction of the first fluid defined as water in each element on the outlet surface. A standard deviation equal to the maximum results in a 0% mixed solution and a standard deviation equal to 0 results in a 100% mixed solution.

The mass fraction simulation results are shown in Figure 6.3. In these contour plots,

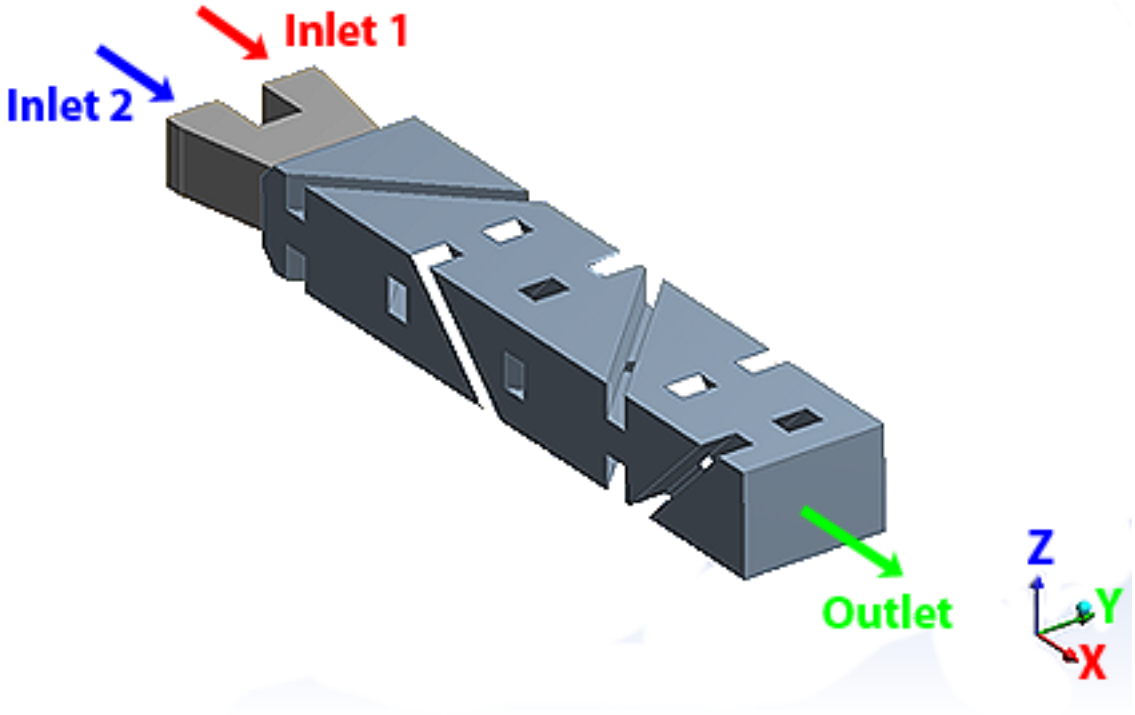

(a)

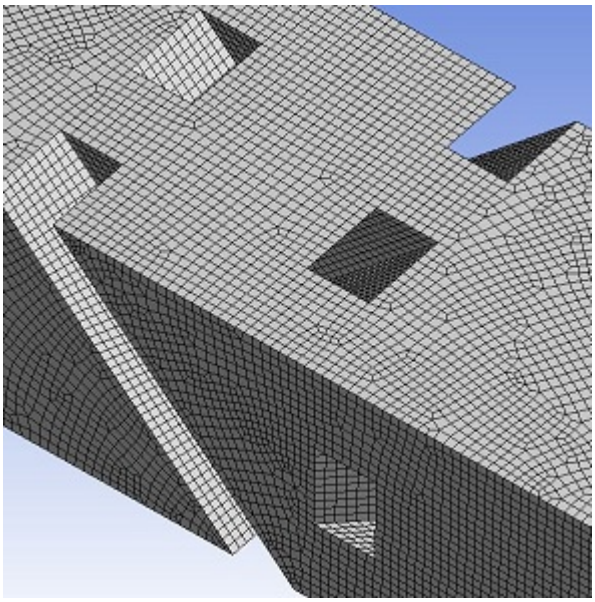

(b)

Figure 6.2: Geometry and Mesh of SMX Style Hose: (a) Overview of Geometry and (b) Enlarged View with Mesh

red represents a mass fraction of 1 (i.e., a cell completely filled with the first fluid), blue represents a mass fraction of 0 (i.e., a cell completely filled with the second fluid), and green represents a mass fraction of 0.5 (i.e., a cell filled with 50% of the first fluid and 50% of the second fluid). Therefore, the mass fraction simulation results for an ideal mixer would show all red entering though the first inlet, all blue entering through the second inlet, and all green exiting the hose. The results show low mixing of 2.0% for the plain hose and 6.4% for the HEV hose, while 59.0% mixing for the two liquids was obtained at the end of the SMX style hose. To verify the simulation results, an experiment was constructed, which is discussed in Chapter 7.

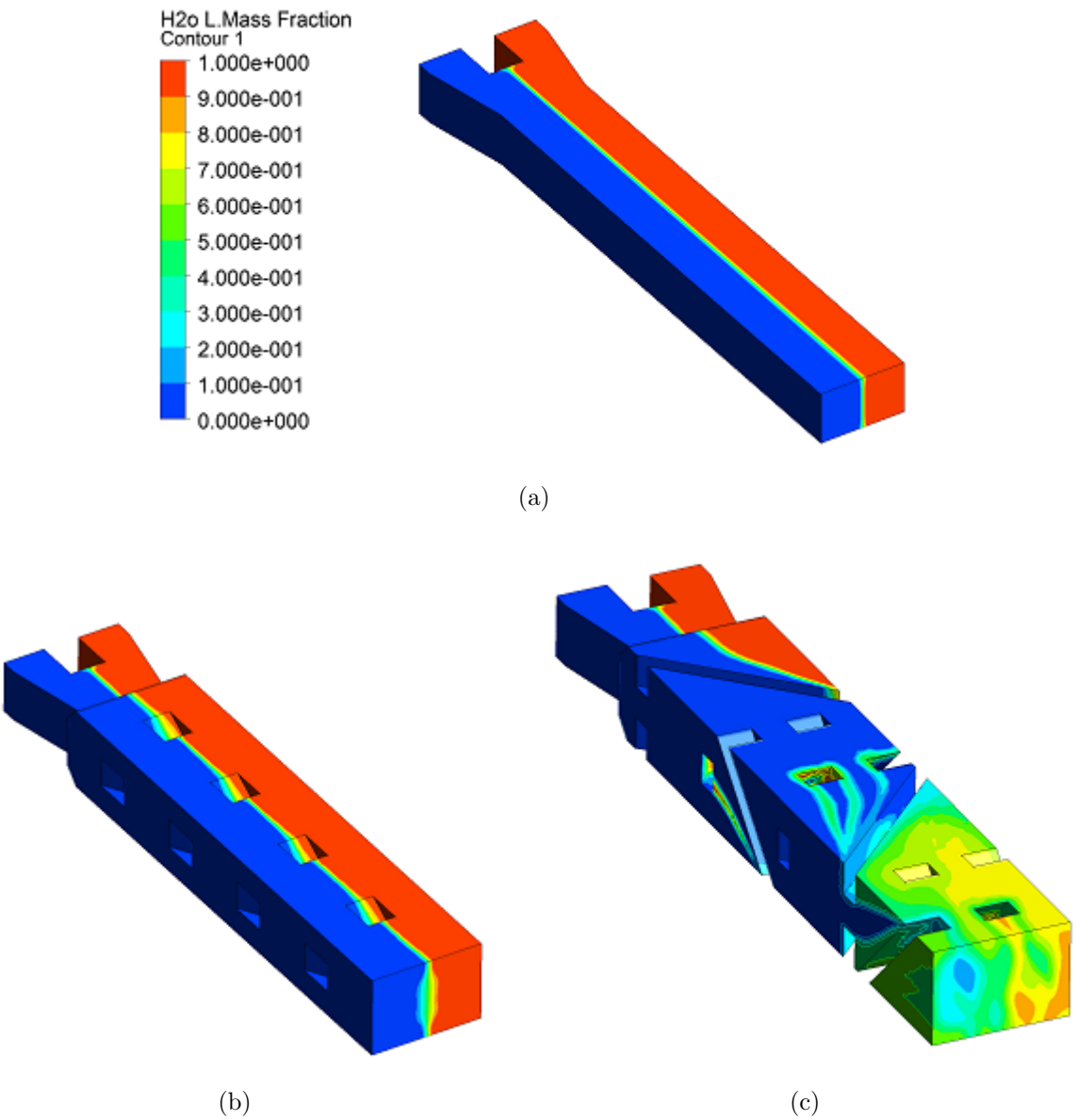

(a)

(b)

(c)

Figure 6.3: Preliminary Simulation Results: (a) Plain Hose (2.0% Mixed), (b) HEV Hose (6.4% Mixed), and (c) SMX Hose (59.0% Mixed)

Chapter 7

Mixing Experiments

To confirm the guidance provided by the numerical simulations, an experiment was constructed to test the different hose designs. Due to the small size of the hose, a color dilution method was used to measure the mixing efficiency of the hose designs. Another reason for using this testing method was that it was less expensive and easier to set up than other methods, such as PLIF (discussed in Section 4.3).

7.1 Experimental Setup

To measure the degree of mixing through each hose, the payload body was used with one reservoir compartment filled with distilled water dyed with black food coloring and the other compartment filled with plain distilled water. The motor was supplied with 4.0 V, a typical voltage level seen by the motor during operation, and the plunger was then actuated until the mixture reached the end of an open channel extension that was added onto the hose. A digital camera mounted above the hose photographed the mixture in the extension once the plunger was stopped. To determine mixing efficiency, the standard deviation of blue channel pixel values from the RGB color image was calculated and used in Equation 4.7. The blue channel was chosen because there was a larger difference between the dyed and undyed liquid pixel values for the blue channel than for the red or green channels. A rectangular region in the open channel extension immediately after the hose exit was used for the measurement. To calculate the maximum standard deviation for each hose, separate photographs of only black dyed water and of only undyed water were used. The pixel values in the measurement region of each photograph were extracted and assumed to be part of the same photograph. The standard deviation of the combined pixel values was taken to

give the maximum standard deviation. The payload body with the open channel extension is shown in Figure 7.1.

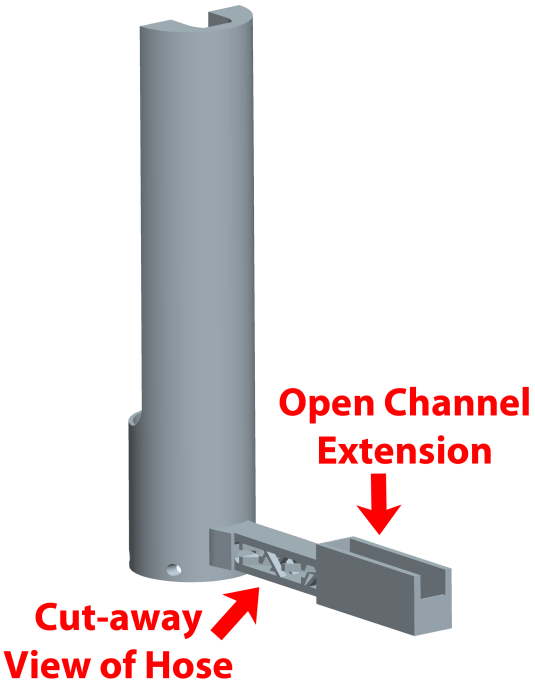

Figure 7.1: Payload Body with SMX Hose and Open Channel Extension Used for Mixing Experiments

The payload body and camera were both mounted in a stand that overhung a laptop computer screen. The computer was opened to 180° and a blank Microsoft Powerpoint document was set in presentation mode which provided diffuse and even illumination. To further diffuse the light, a rectangular piece of white Delrin plastic was mounted just below the hose. All overhead lights were switched off during testing. A schematic of the experimental setup is show in Figure 7.2.

7.2 Modified Simulation Setup

In Chapter 6, preliminary simulation setup and results were discussed. The mixing efficiencies for those hose designs were calculated using a surface perpendicular to the bulk flow direction, immediately at the end of each hose (outlet surface in Figure 6.2(a)). However, the experiment calculates mixing efficiency based on a rectangular region parallel to the bulk

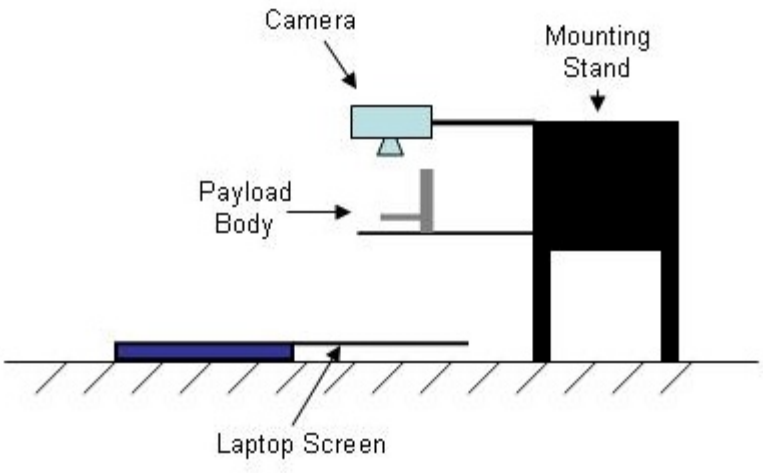

Figure 7.2: Schematic of Experimental Setup

flow direction. In addition, the camera only captures a 2D photograph of the distribution of the black dye whereas the simulation is able to produce mass fraction data in three dimensions. Therefore, the simulation setup and mixing efficiency calculation region were slightly modified to produce a situation closer to the experiment than the situation created by the preliminary simulation setup.

To reproduce the mixing hose extension used in the experiment, an extension was also added to the end of the hose in the simulation. An example of this extension is shown in Figure 7.3. The hose orientation with respect to gravity, as shown in Figure 6.2, remained the same for the modified simulation so that the simulation and experiment would be consistent.

To verify the simulation using the experimental setup described above, a similar measurement needed to be taken in both the experiment and the simulation. To accomplish this, the mass fraction data from the simulation were manipulated to reflect the measurement taken by the camera in the experiment. First, a rectangular region at the beginning of the hose extension similar in size to the region used in the experiment was selected. This region is labeled in Figure 7.3 as the Measurement Region. Due to the mesh type and size used in the simulation, mass fraction data were available at 0.1 mm increments in each direction inside the measurement region. Next, at each (X,Y) location inside the measurement region, the mass fraction data were averaged along the Z-direction. This type of averaging results in a

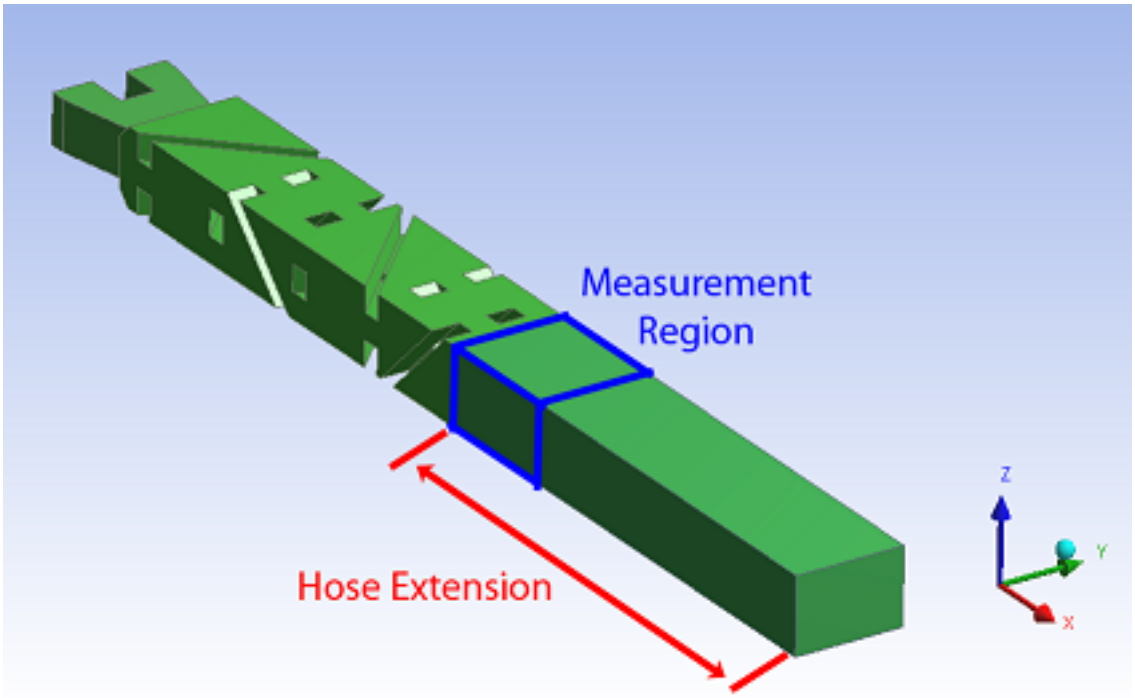

Figure 7.3: SMX Style Hose with Extension used in the Modified Simulations

planar surface with a single mass fraction value at each (X,Y) location. Because the camera in the mixing experiment captures a 2D representation of the distribution of black dye in the hose extension and the mass fraction data from the simulation was manipulated to give a 2D representation as well, these two measurements were assumed to be similar.

Using this modified setup, simulations were run using the plain hose, HEV style hose, SMX style hose, and a double length SMX style hose. As in the preliminary simulations, two liquids, both defined as water, were used as the working fluids for each hose. Because one possible application of the liquid delivery payload is to deliver a fibrin sealant (which has two different liquid components), additional simulations were run for the plain hose and SMX style hose using water as the first liquid and a glycerin–water mixture as the second liquid. A glycerin–water mixture was used to create the second liquid because its properties were known [68]. A composition of 50% by volume glycerin and 50% by volume water was chosen for the glycerin–water mixture and results in a liquid that has a density of 1129 kg/m^3 and a dynamic viscosity of $4.66 \cdot 10^{-3}$ Pa·s [68]. This composition was chosen because it was easily applied in the experiment. Water has a similar vicosity to the thrombin solution and

the viscosity of the fibrinogen solution in a typical fibrin sealant is 0.030 Pa·s.

7.3 Simulation and Experimental Results

The simulation and experimental results for the plain hose using water as both working fluids are shown in Figure 7.4. Three trials with the plain hose are shown in Figure 7.4(b) along with their associated standard deviation of pixel values for the blue channel. The yellow rectangles in these photographs represent the measurement regions.

The simulation predicted almost no mixing with the plain hose because the two liquids simply flow side–by–side through the hose. Only a very small amount of mixing occurred at the two–liquid interface resulting in a mixing efficiency of 2.4%. In the experiment, the same side–by–side flow pattern was observed. Averaging the standard deviations from the three trials resulted in a mixing efficiency of 4.5% ± 1.3% for the plain hose ($\sigma_{max} = 37.0$) which is similar to the efficiency predicted by the simulation.

The HEV style hose was the second hose tested, and the simulation and experimental results are shown in Figure 7.5. The simulation predicted a side–by–side flow structure similar to that of the plain hose but with slightly more mixing at the two-liquid interface. The predicted mixing efficiency was 6.0%. A similar flow structure was seen in the experiment along with a similar mixing efficiency of 5.3% ± 1.5% ($\sigma_{max} = 33.5$).

Figure 7.6 shows the simulation and experimental results for the third hose, the SMX style hose. The simulation predicted stripe–like structures of commonly–valued mass fraction cells and a mixing efficiency of 64.8%. The experimental results show similiar stripe–like features and a similar mixing efficiency of 70.0% ± 0.8% ($\sigma_{max} = 46.0$).

The fourth hose is also an SMX style hose; however, it is twice as long as the previous SMX style hose. The plot in Figure 7.7(a) shows mostly green contours indicating a mass fraction of 0.5 in many of the cells and a well mixed case. The predicted mixing efficiency was 86.0%. The experiment also resulted in a well mixed case with a few faint streaks. The mixing efficiency from the experiment was 87.5% ± 0.1% ($\sigma_{max} = 27.2$).

In addition to using water as both working fluids, the plain hose and the SMX style hose were simulated and tested using water as the first fluid and a glycerin–water mixture as the

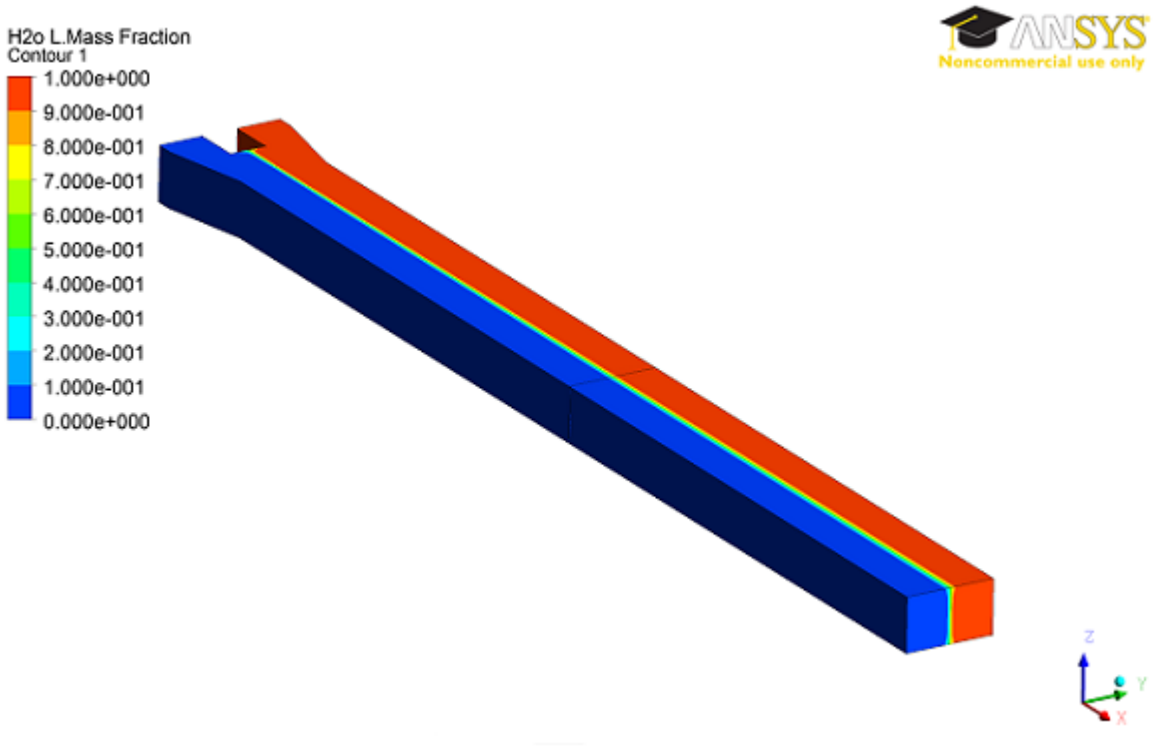

(a)

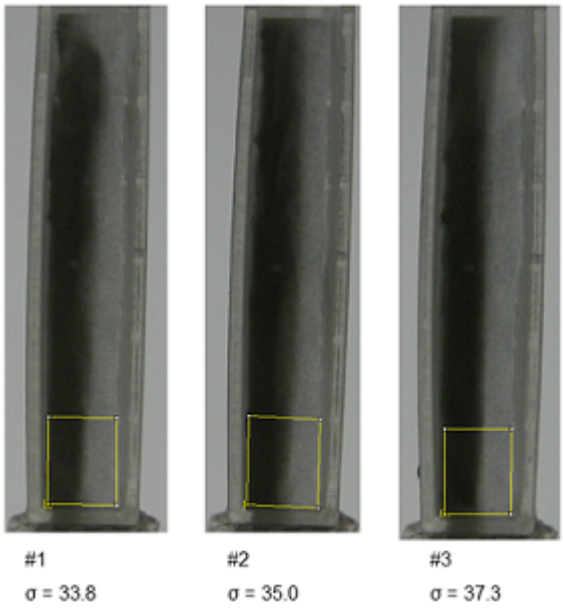

(b)

Figure 7.4: Plain Hose Results Using Water as Both Working Fluids: (a) Simulation and (b) Experimental Results

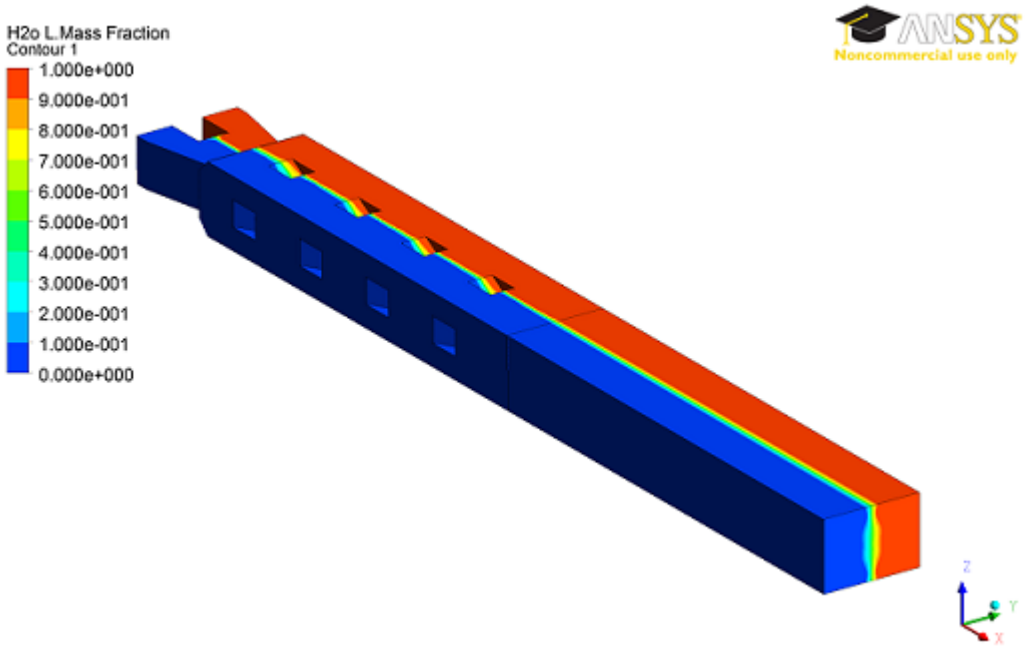

(a)

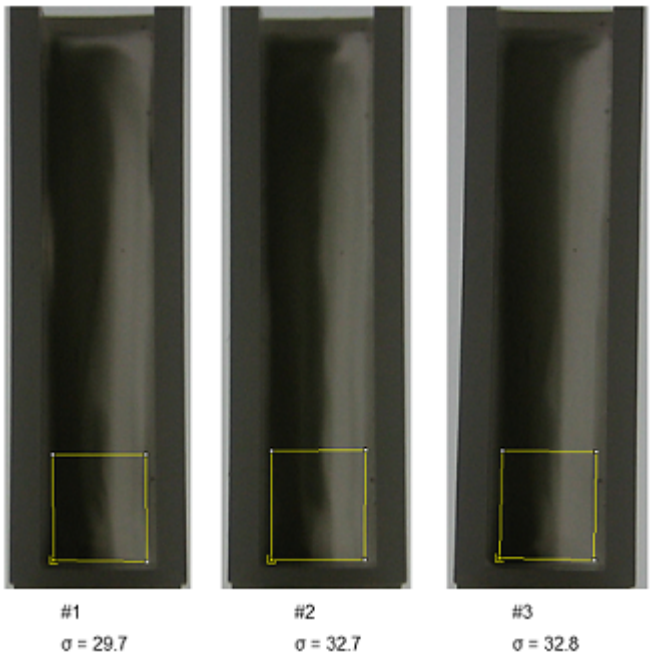

(b)

Figure 7.5: HEV Hose Results Using Water as Both Working Fluids: (a) Simulation and (b) Experimental Results

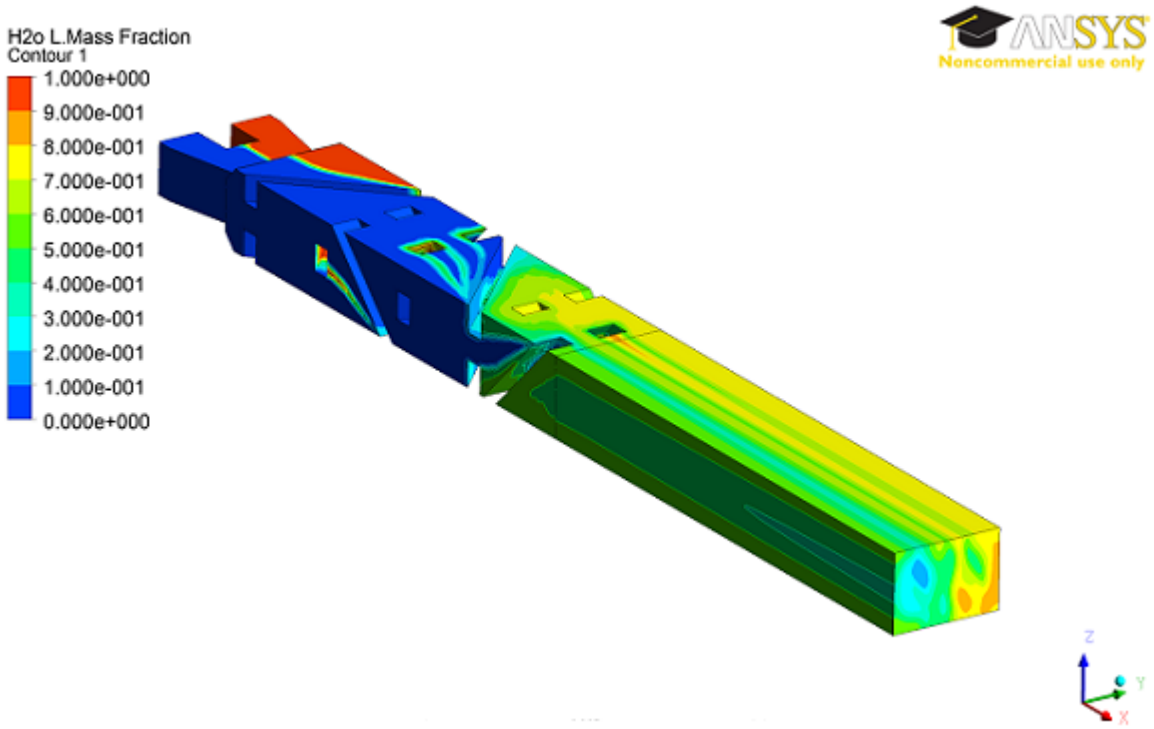

(a)

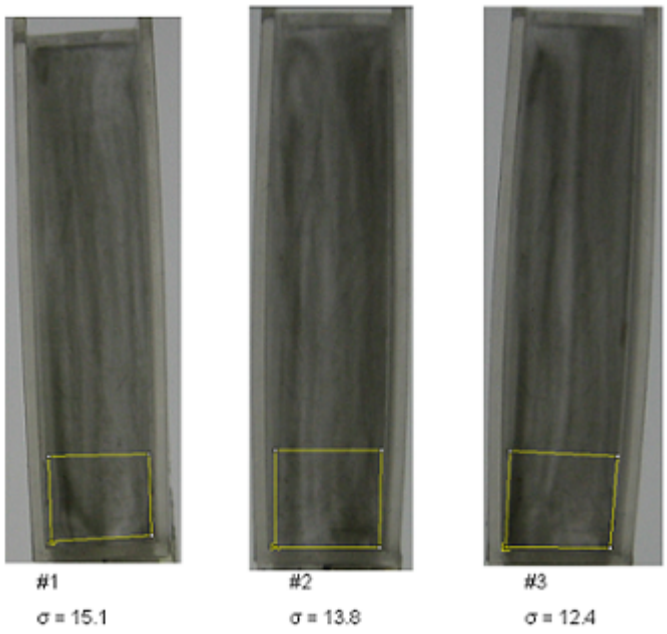

(b)

Figure 7.6: SMX Hose Results Using Water as Both Working Fluids: (a) Simulation and (b) Experimental Results

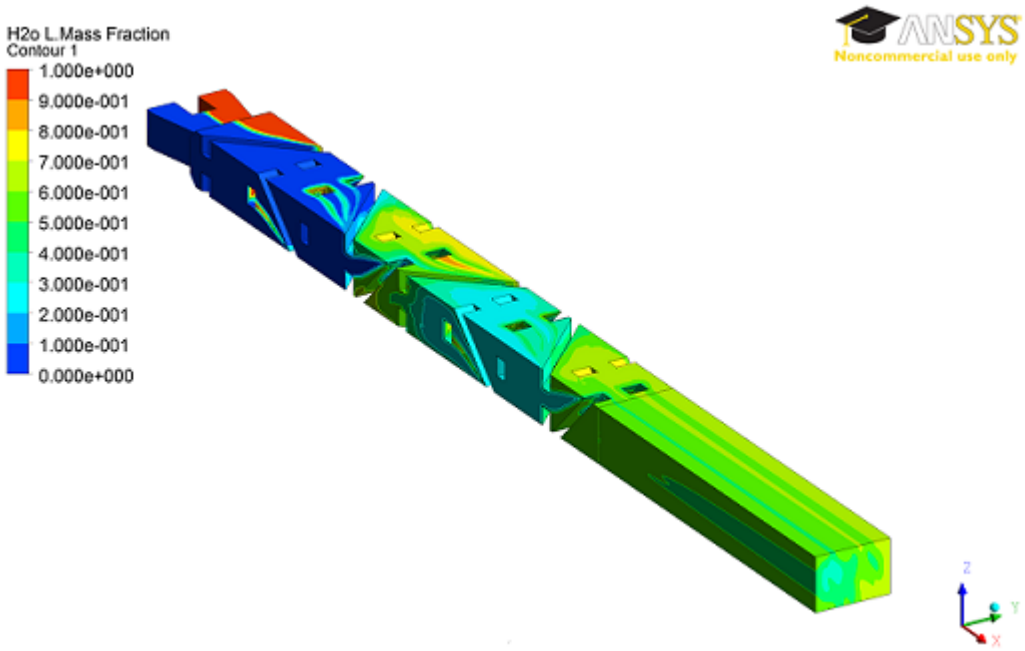

(a)

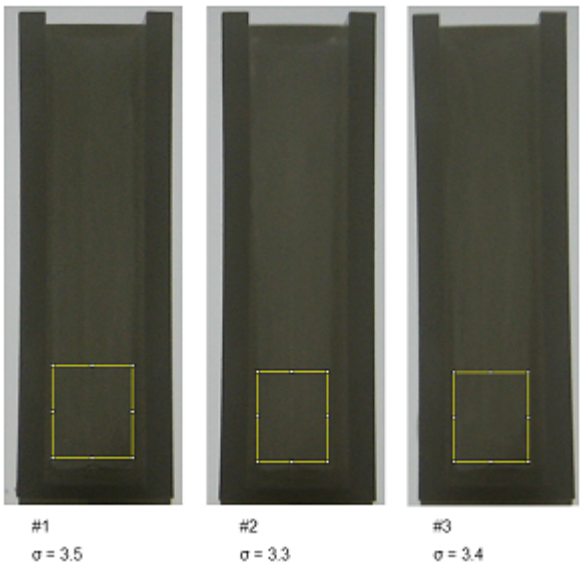

(b)

Figure 7.7: SMX Double Length Hose Results Using Water as Both Working Fluids: (a) Simulation and (b) Experimental Results

second fluid. In the experiment, the distilled water was dyed black and the glycerin–water mixture was left clear.

The simulation and experimental results for the plain hose using water and the glycerin–water mixture are shown in Figure 7.8. The contour plot from the simulation in Figure 7.8(a) shows almost no mixing with a distinct separation between the water and the glycerin–water mixture. The water quickly floats to the top and the glycerin–water mixture quickly sinks to the bottom of the hose. However, using the measurement method described in Section 7.2, a mixing efficiency of 99.2% is predicted. The experiment showed a completely uniform mixture resulting in a mixing efficiency of 93.0% which is similar to the simulation's prediction. However, taking a side–view photograph of the experiment (Figure 7.8(c)), the same separated flow structure as predicted by the simulation can be seen, which is clearly not approximately 95% mixed. In addition, if the standard deviation in the simulation was calculated in the measurement region without averaging the mass fraction values along the Z–direction (i.e., using every mass fraction value in the measurement region in 3D), the mixing efficiency is predicted to be 8.0% which is much more reasonable considering the flow structure. These results indicate that the experimental method used is not suitable for measuring mixing between two different liquids. Because the camera captures a 2D representation of the 3D distribution of black dye, the RGB pixel values in the image are a line–of–sight average. If two liquids with different densities and viscosities are used in the experiment, the less dense liquid is pushed on top of the more dense liquid forming a layered structure. The camera takes a line–of–sight average of the layered structed and the distrubition of black dye appears to be homogenous. Therefore, using two different liquids with the existing experimental method gives an incorrect measurement of mixing efficiency.

A similar conclusion about the experimental method using two different liquids was reached based on simulations and tests of the SMX style hose using water and the glycerin–water mixture. The simulation and experimental results for this case are shown in Figure 7.9. Using the measurement method described in Section 7.2, a mixing efficiency of 92.4% was predicted by the simulation. However, the contour plot of the simulation results showed layers of commonly valued cells in the X–Y plane and did not appear to be well mixed. The experiment showed similar results to the simulation with a mixing efficiency of 91.2%.

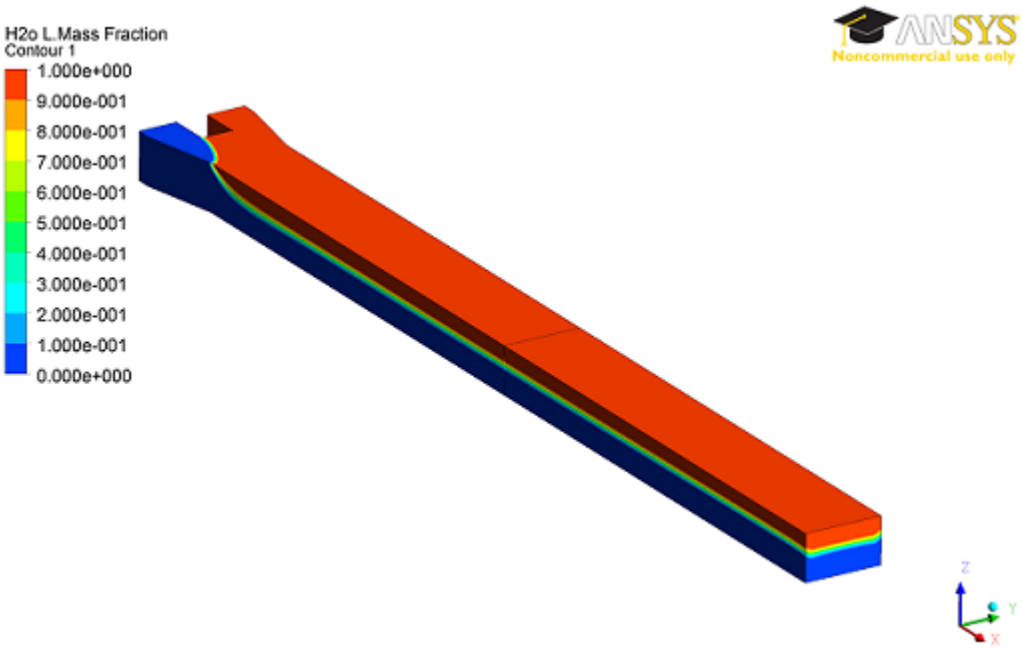

(a)

(b)

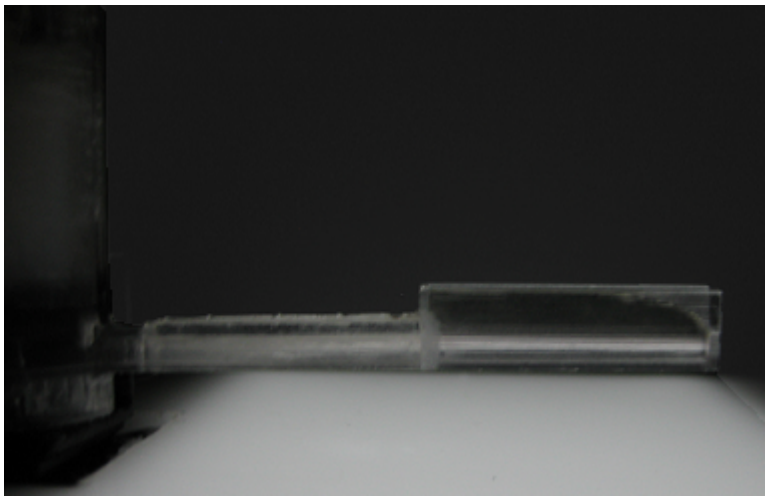

(c)

Figure 7.8: Plain Hose Results Using Water as the First Working Fluid and a Glycerin–Water Mixture as the Second Fluid: (a) Simulation and (b) Experimental Results; (c) Side View of Experimental Results

Again, a side view of the hose showed a layered structure in the horizontal plane matching the simulation's prediction. As with the plain hose case, if the standard deviation in the simulation was calculated without averaging along the Z–direction, a mixing efficiency of 31.8% was predicted which is also more reasonable considering the flow structure.

7.4 Discussion

An experiment was designed and carried out to validate the mixing efficiency results from the numerical simulation. Four different cases were tested with water as both of the working fluids, and two different cases were tested using water as the first working fluid and a glycerin–water mixture as the second working fluid. In all four cases using water as both working fluids, the simulation and experimental results were similar. In the two cases using water and a glycerin–water mixture as the working fluids, the experimental method gave incorrect results. However, the layered flow structure was visually similar in both the simulation and experiment. Therefore, it was concluded that the simulation was providing accurate results. Because the simulation results were validated by the physical experiments, different hose designs could be explored using simulation alone and without performing time–consuming and expensive experiments. Other designs for the mixing hose explored using simulation are presented in Chapter 8.

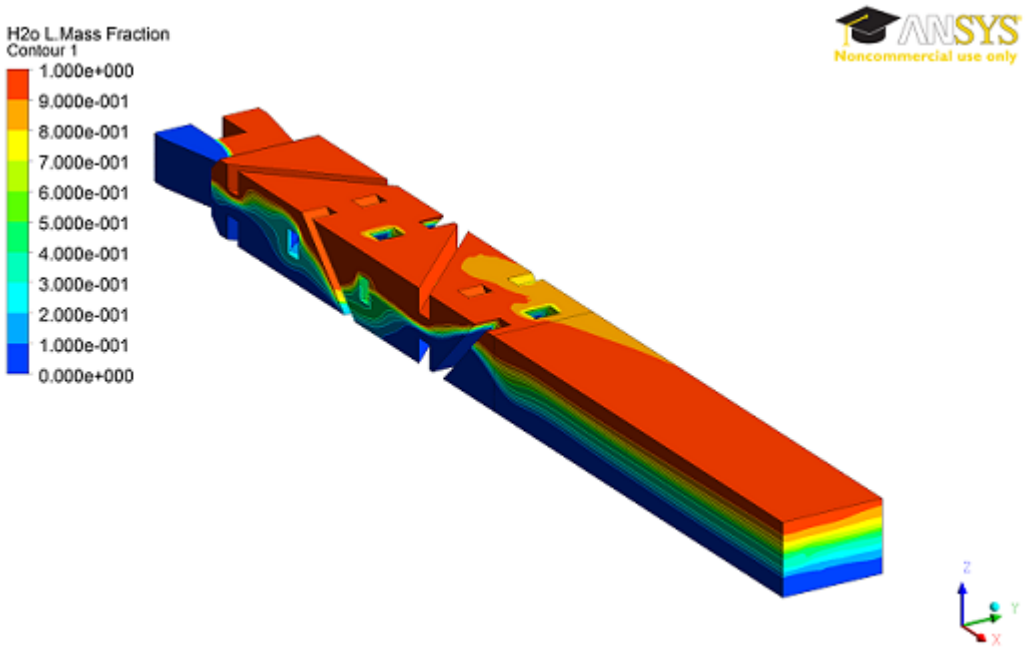

(a)

(b)

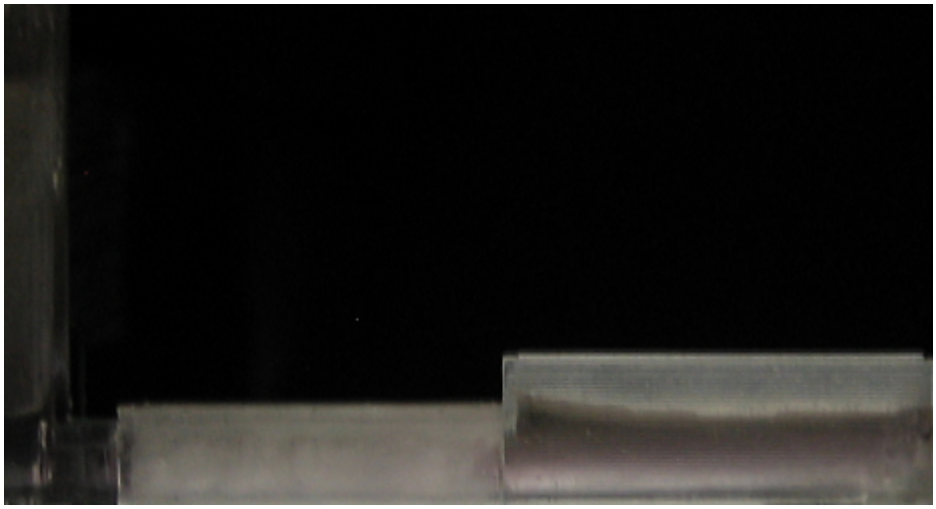

(c)

Figure 7.9: SMX Style Hose Results Using Water as the First Working Fluid and a Glycerin–Water Mixture as the Second Fluid: (a) Simulation and (b) Experimental Results; (c) Side View of Experimental Results

Chapter 8

Exploration of Mixing Hose Design

Results from the ANSYS Fluent 12.1 simulations were verified for six different cases and discussed in Chapter 7. Because the simulation was experimentally validated, it was then used to explore additional designs that might improve mixing in the hose. One possible application of the liquid delivery payload is to assist with hemostasis by delivering a fibrin sealant. Therefore, the following simulations used viscosities similar to those of the two components in a typical fibrin sealant.

8.1 Simulation Setup

Two simple modifications were made to the simulation setup. First, the orientation of the hose was rotated 90° about its long axis (i.e., gravity pointed in the negative Y–direction instead of the negative Z–direction). In the previous simulations and the experiment, the mixing hose was laid on its side to allow for a matching orientation between the simulation and experiment. However, when an incorporeal robot is equipped with a liquid delivery payload, the exit ports are orientated one above the other instead of side–by–side. Therefore, the following simulations used the new orientation. Figure 8.1 shows the new orientation used.

Second, water was still used as the first liquid but a different glycerin–water mixture was used for the second liquid. This mixture was 70% by volume glycerin and 30% by volume water, which resulted in a viscosity of 0.030 Pa·s [68]. Water has a similar vicosity to the thrombin solution and the new glycerin–water mixture has a similar viscosity to the fibrinogen solution in a typical fibrin sealant.

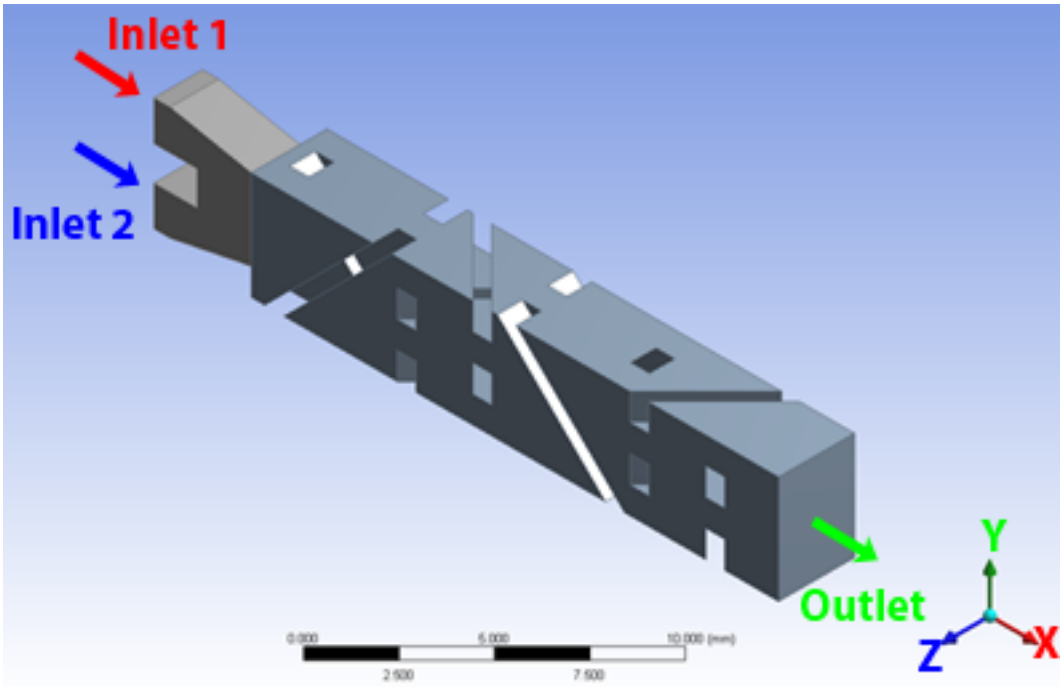

Figure 8.1: SMX Style Hose in Rotated Orientation

8.2 Simulation Results

With the new hose orientation (Figure 8.1), the inlets are position one above the other and the choice of inlet for the water component is important because gravity has a larger affect on mixing than when the inlets are positioned side–by–side. The first two simulations were run with the SMX style hose to determine which inlet the water component should enter through. These results are shown in Figure 8.2. When water enters through Inlet 2, the mixing efficiency at the hose outlet is 67.0%, which is more than double the mixing efficiency when water enters though Inlet 1, 31.8%. Therefore, the water component was setup to enter through Inlet 2 for the remaining simulations.

Next, the SMX style hose was compared with two different hose styles. The first hose style has helical elements similar to the Kenics KM mixer (Figure 4.1(a)) and the second hose has thin SMX style blades. The helical elements were cut to fit the same cross–sectional size as the SMX style hose. The blade thickness of the SMX style hose was reduced to 0.4 mm from 1.0 mm. Cut–away views of both hose designs are shown in Figure 8.3 and simulation results are shown in Figure 8.4. The resulting mixing efficiencies for the helical hose and the

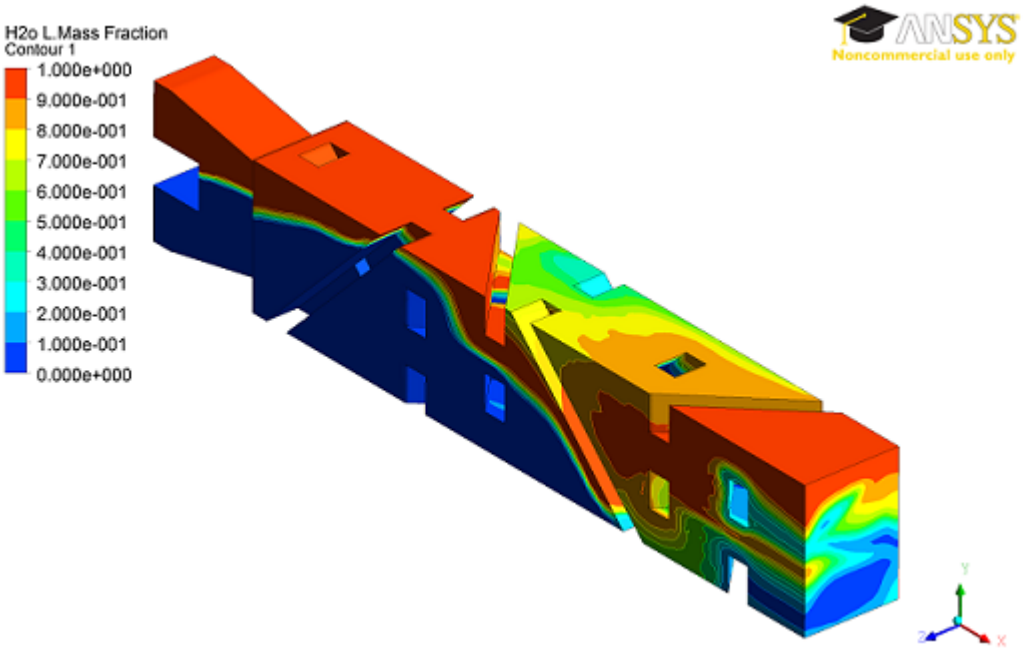

(a)

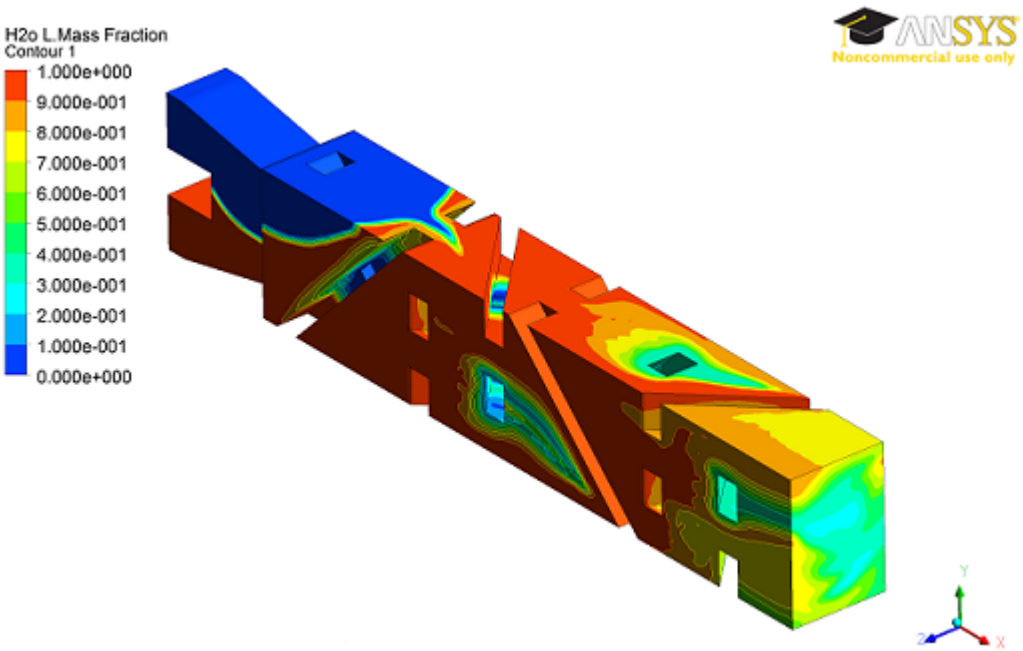

(b)

Figure 8.2: Simulation Results for SMX Style Hose with Water Component Entering Through: (a) Inlet 1 (31.8% Mixed) and (b) Inlet 2 (67.0% Mixed)

thin SMX hose are 48.6% and 40.4%, respectively. With a mixing efficiency of 67.0%, the original SMX style hose still performed better than the helical and thin SMX style hoses.

Another set of hose designs were simulated to see if they could perform better than the original SMX style hose. These two hoses were a combination of helical elements and SMX style blades. In the first hose of this new set, the helical–SMX hose, two helical elements were followed by two SMX style blade elements. In the second hose, the SMX–helical hose, the order of these elements were reversed compared to the helical–SMX hose. Cut–away views of these hose designs are shown in Figure 8.5 and simulations results are shown in Figure 8.6. Both of these hose designs resulted in a very similar mixing efficiency and also did not perform as well as the original SMX style hose. The mixing efficiencies for the helical–SMX hose and the SMX–helical hose were 62.2% and 62.4%, respectively.

Of the new hose designs simulated, the SMX style hose produced the highest mixing efficiency at the outlet. Therefore, it was recommended that this style hose be used when two liquids need to be mixed before being dispensing. The next set of simulations investigated how a faster or slower inlet velocity affected mixing through the SMX style hose. One simulation was run with an inlet velocity of 70.4 mm/s and the other used an inlet velocity of 8.8 mm/s corresponding to a factor of four increase and a factor of two decrease compared to the original velocity used, respectively. The faster velocity simulates using a motor with a 64:1 instead of a 256:1 gearhead. The slower velocity simulates running the 256:1 gearhead and motor at half of the speed used previously. The simulation results are shown in Figure 8.7. With a faster inlet velocity, a spot of darker blue remained at the top and a spot of orange remained at the bottom of the hose outlet. With a slower inlet velocity, there was a dark blue region at the bottom and a red region at the top of the hose outlet. The increase in velocity appeared to help keep the more dense liquid (blue) at the top of the hose and the decrease in velocity appeared to allow the more dense liquid to sink to the bottom of the hose. Both of the resulting mixing efficiencies were lower than the mixing efficiency when using a inlet velocity of 17.6 mm/s. The faster inlet velocity of 70.4 mm/s resulted in a mixing efficiency of 65.4% and the slower inlet velocity of 8.8 mm/s resulted in a mixing efficiency of 41.2%.

The simulation results showed that the SMX style hose with an inlet velocity of 17.6

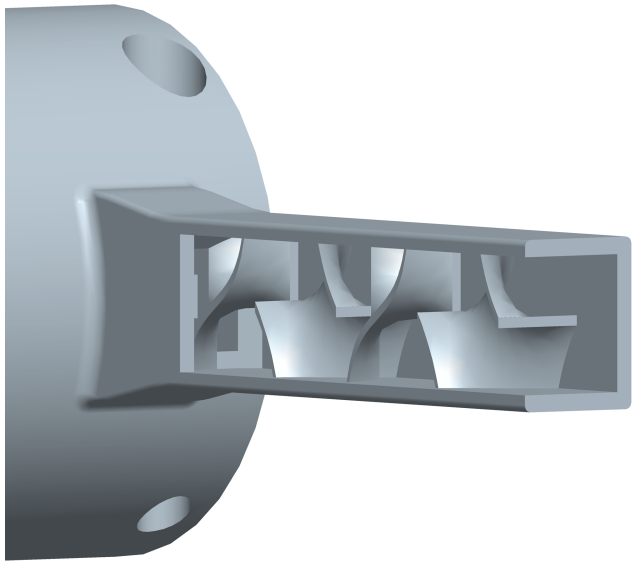

(a)

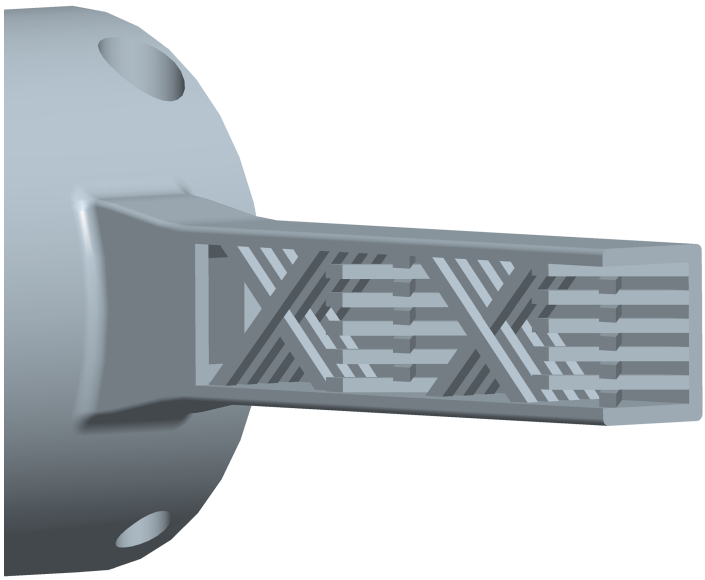

(b)

Figure 8.3: Cut–away View of Hose Designs: (a) Helical and (b) Thin SMX Style Hoses

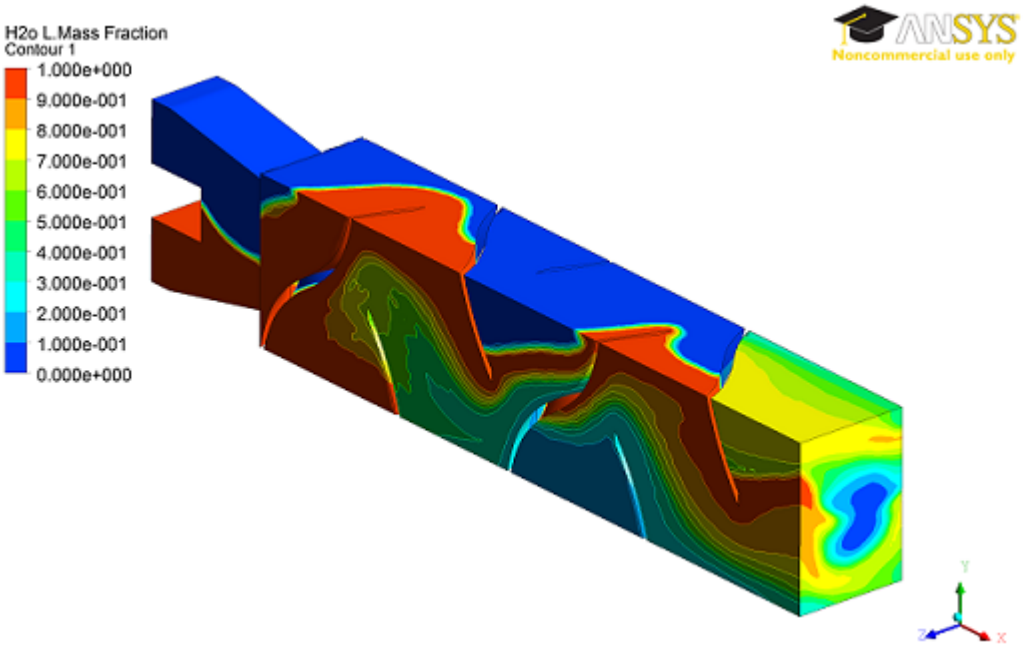

(a)

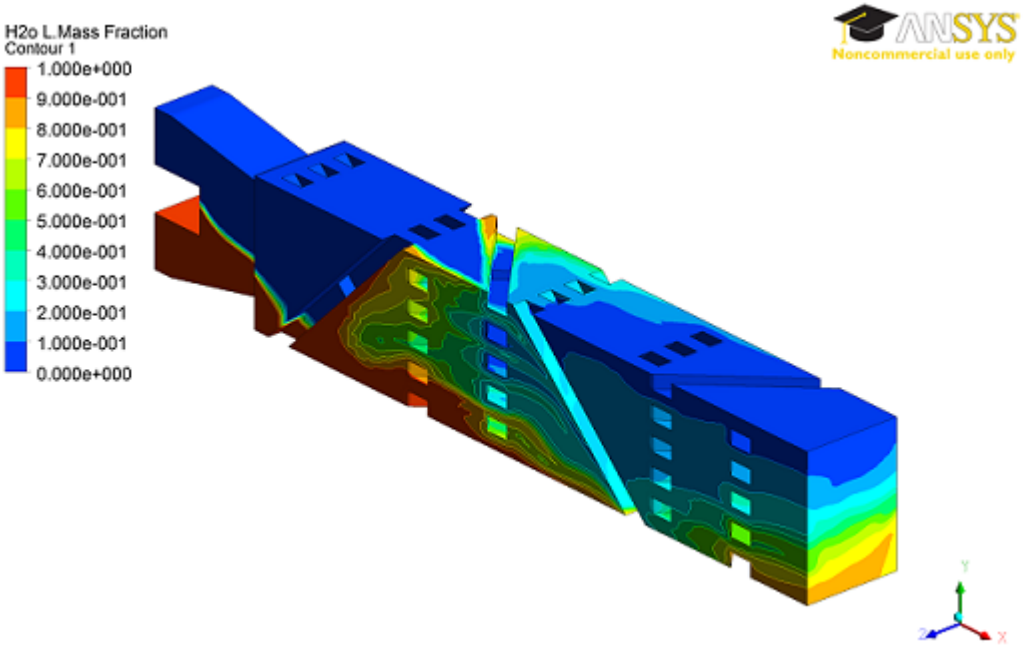

(b)

Figure 8.4: Simulation Results for: (a) Helical (48.6% Mixed) and (b) Thin SMX Style(40.4% Mixed)

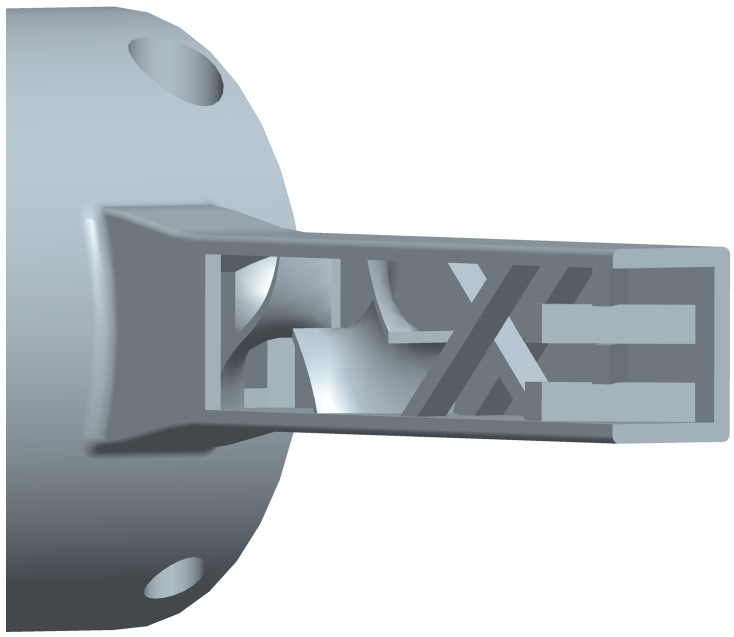

(a)

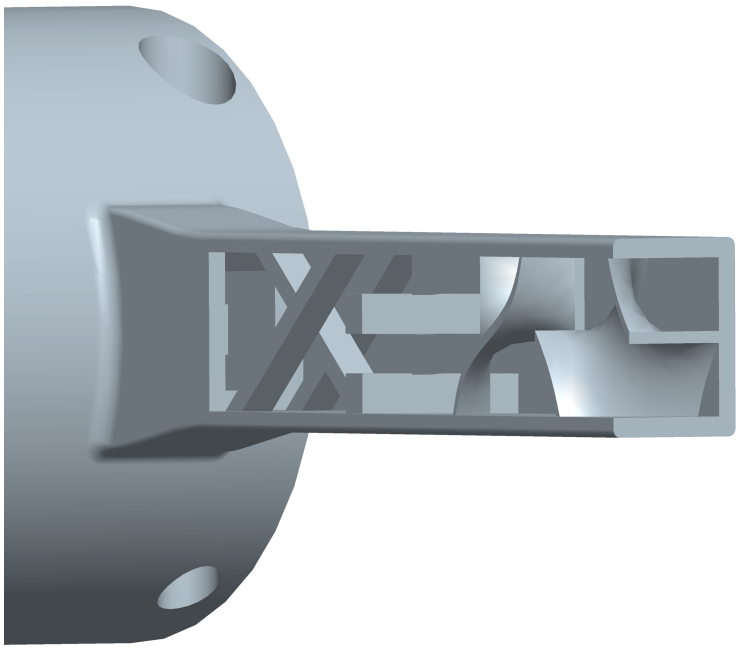

(b)

Figure 8.5: Cut–away View of Hose Designs: (a) Helical–SMX and (b) SMX–Helical Hoses

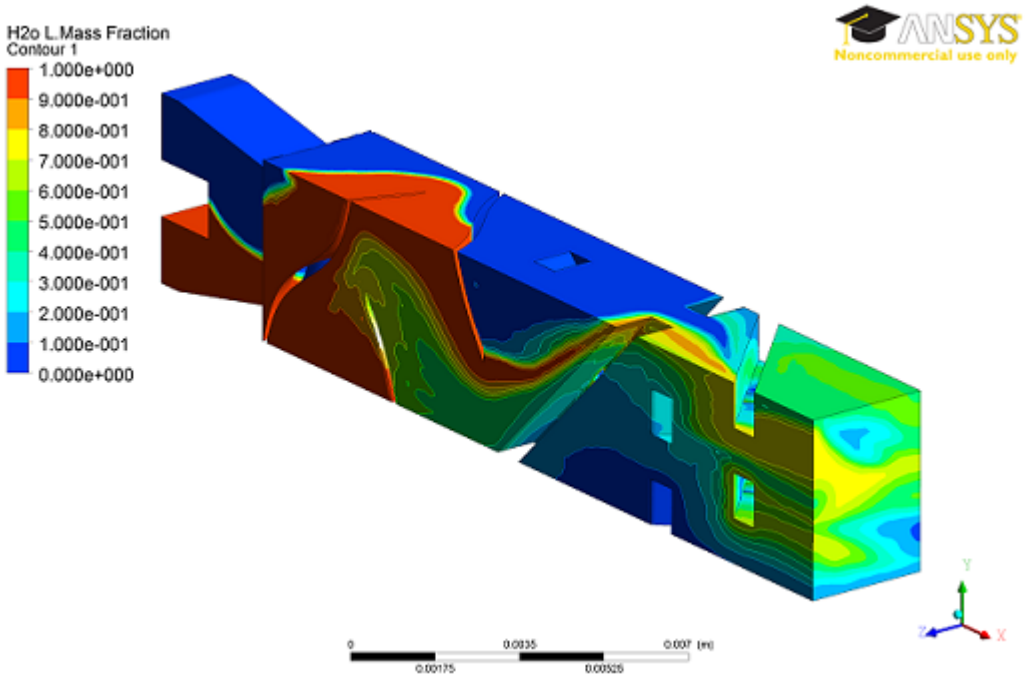

(a)

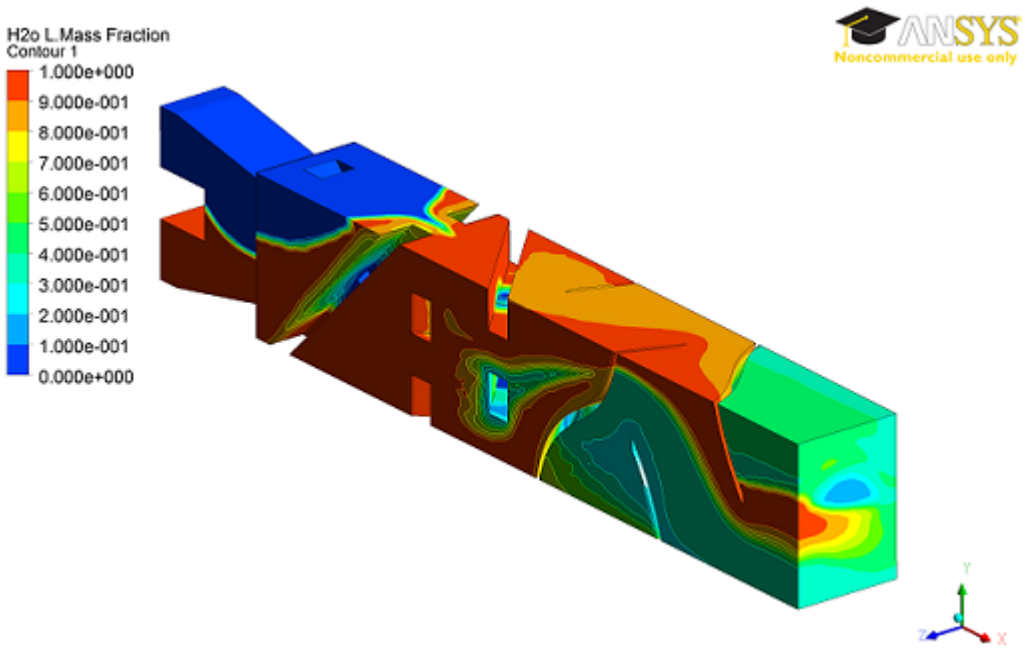

(b)

Figure 8.6: Simulation Results for: (a) Helical–SMX (62.2% Mixed) and (b) SMX–Helical (62.4% Mixed)

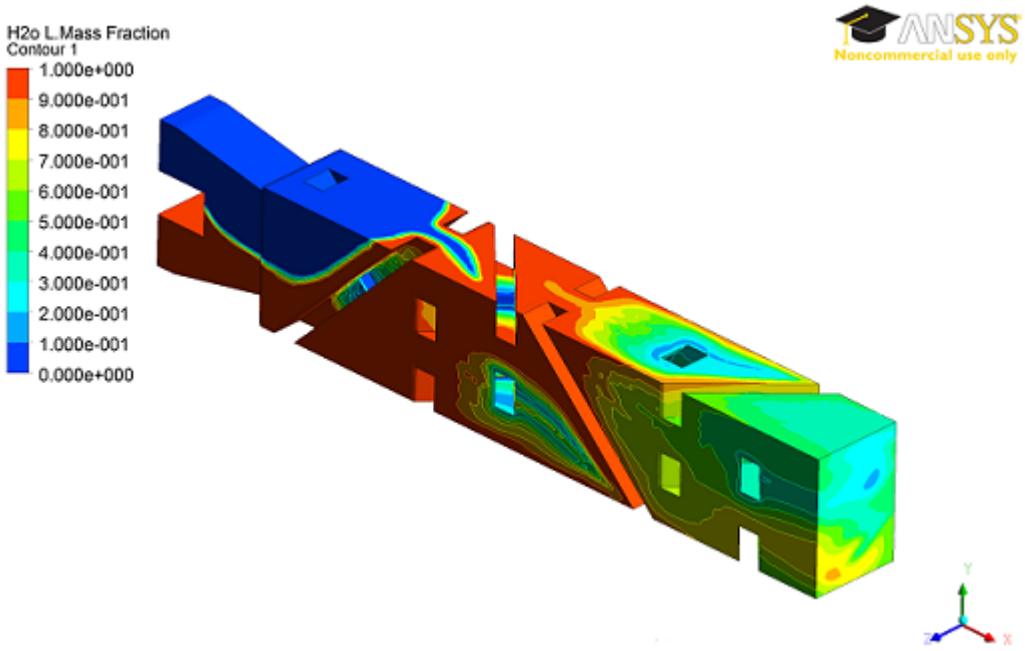

(a)

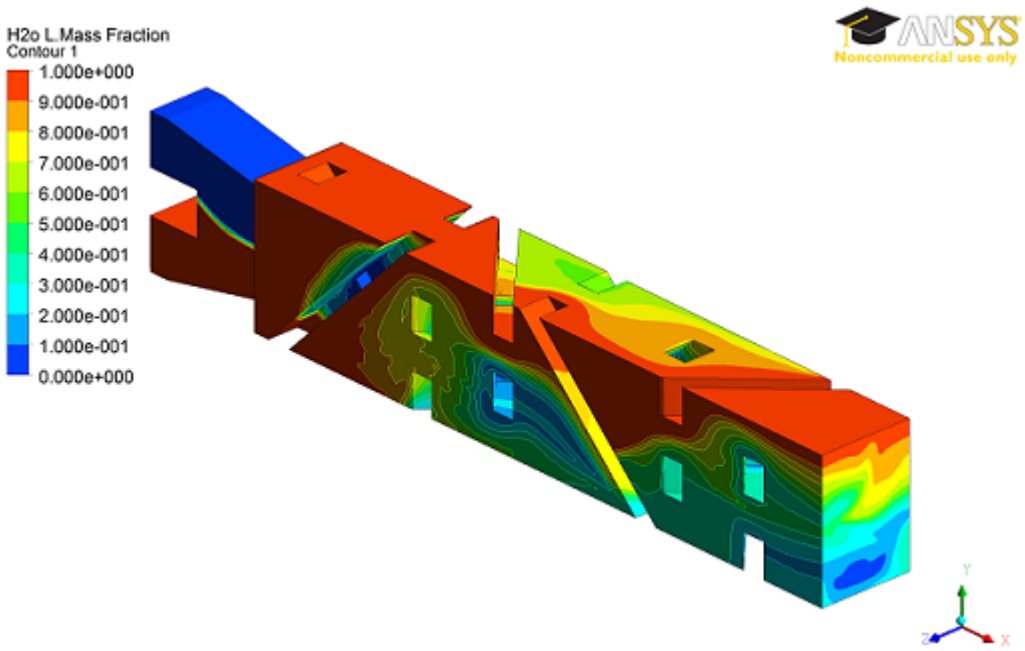

(b)

Figure 8.7: Simulation Results for: (a) Factor of Four Increase (65.4% Mixed) and (b) Factor of Two Decrease in Inlet Velocity (41.2% Mixed)

mm/s reached the highest mixing efficiency of the group at the hose outlet (67.0%). This was considered good performance because the viscosities of the two fluids differ by a factor of 30, and the hose is only 4.0 mm high, 2.8 mm wide, and 18.0 mm long. However, a final simulation was run to explore whether mixing efficiency would improve by doubling the length of the hose. The results in Figure 8.8 show an almost completely green–colored outlet corresponding to a mxing efficiency of 90.0%.

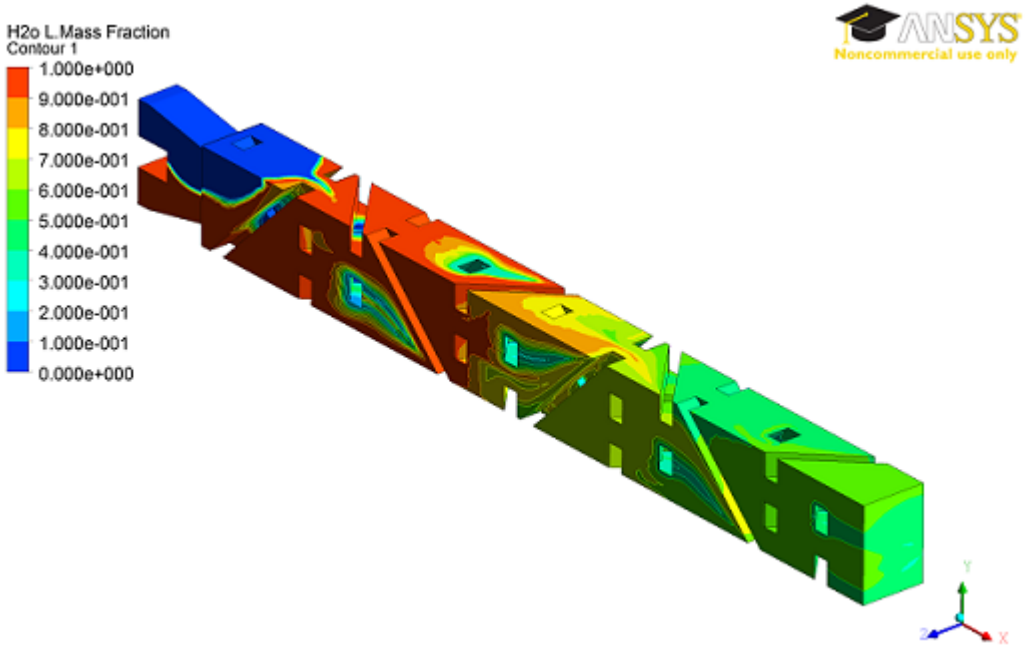

Figure 8.8: Simulation Results for the Double Length, SMX Style Hose (90.0% Mixed)

8.3 Conclusions

Additional simulations were performed and rated based on mixing efficiency at the hose outlet. All of these simulations used a rotated hose orientation with respect to the orientation used in Chapter 7. The hose was rotated to match the actual orientation used when dispensing liquid. Also, the second liquid component was changed to a glycerin–water mixture with a viscosity of 0.030 Pa·s. The first liquid component remained water with a viscosity of 0.001 Pa·s.

Using the SMX style hose, it was found that if the second liquid component entered through Inlet 1 instead of Inlet 2, the mixing efficiency increased from 31.8% to 67.0%. Using this inlet setup, four additional hose designs were simulated. The simulation results for these hoses showed lower mixing efficiencies than for the SMX style hose. Then, taking the SMX style hose as the best performer of the group, two simulations were run using an increased and a decreased inlet velocity. Increasing the inlet velocity by a factor of four or decreasing the inlet velocity by a factor of two resulted in a lower mixing efficiency. Therefore, the SMX style hose using an inlet velocity of 17.6 mm/s was considered to perform well especially considering its small size. If a mixing efficiency higher than 67.0% is desired, it was shown that doubling the length of the SMX style hose resulted in a mixing efficiency of 90.0%. The high mixing efficiency produced by the SMX style hose confirms the third payload design criteria from Section 2.3 was met.

Chapter 9

Porcine Model Testing

9.1 Test Setup

Two incorporeal robots with a fluid delivery payload and SMX style hose were assembled, the reservoir compartments were filled with liquid, and then shipped to the Advanced Medical Technologies Laboratory at the University of Colorado to be tested in an *in vivo* porcine model. After arrival at the University of Colorado, the filled robots were stored for five days prior to testing. The purpose of porcine model testing was to demonstrate the sealing, dispensing, and mixing capabilities of the liquid delivery payload. Because the robots were assembled and filled before being shipped, tape was placed over the hose ends and charging ports prior to shipping to prevent leakage through the open orifices. The liquid used in the robots was made by diluting 1 ml of paint into 180 ml of water. Black paint was used for the first compartment and white paint was used for the second compartment. This mixture was used to provide a color contrast to the internal organs and tissue of the porcine. Also, the white and black liquids would mix to from a gray liquid and a qualitative measure of mixing could be determined. After five days of storage, the robots were placed into the porcine where the plungers were actuated until all of the liquid inside of the reservoirs were expelled.

9.2 Test Results

Upon arrival at the University of Colorado, the robots were inspected and found to be leak–free. In addition, there was no leakage during the five days prior to the test. These findings further confirmed that the payload design is indeed leak–free. Once inside the animal, the

plungers were actuated and liquid was successfully expelled from the reservoirs onto the internal organs. However, the expelled liquid was clear instead of black or white because the paint and water had separated during storage prior to testing. A photograph of the incorporeal robot with a liquid delivery payload during the porcine model test is shown in Figure 9.1.

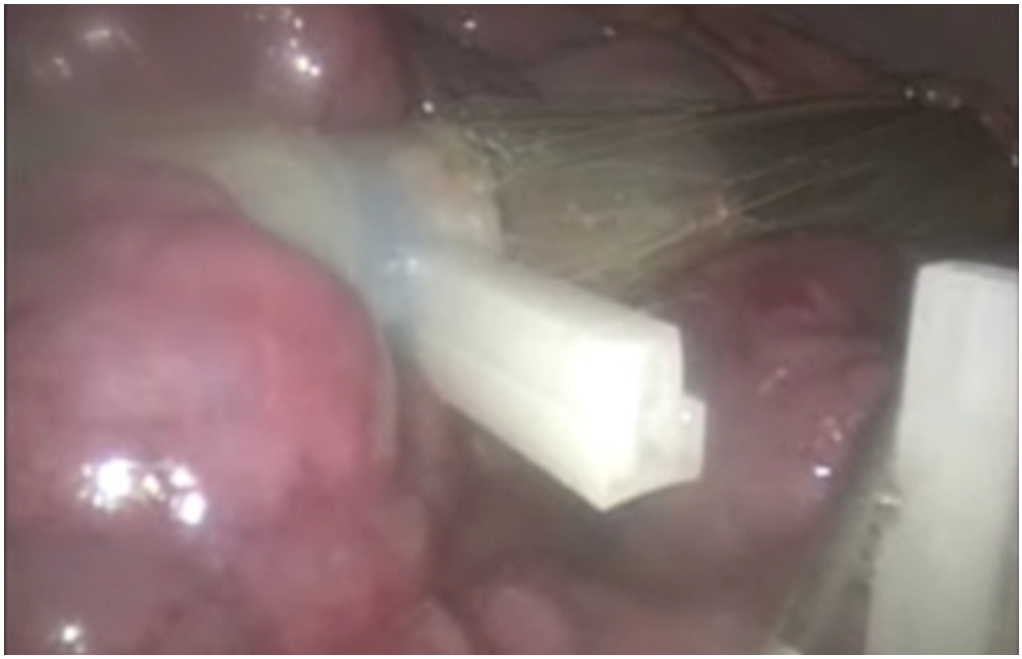

Figure 9.1: Photograph of Incorporeal Robot with Liquid Delivery Payload During Porcine Test

9.3 Discussion

The results from the *in vivo* porcine model confirmed the first and second payload design criteria from Section 2.3 were met. Because the robots were found to be leak–free after shipping and five days of storage, the first design criteria of a sealed chamber had been met. In addition, the robots successfully dispensed liquid from the reservoir onto the porcine organs confirming that the second design criteria had been met.

Chapter 10

Main Control Board Update

10.1 Hall Effect Switch

As discussed in Section 2.3, initial designs of the modular robots required about 30 minutes of assembly immediately prior to use because the only way to turn the robot on or off was by soldering wires to the main control board. This last minute assembly prevents the robots from being tested immediately before an experiment, is a potential source of last minute failures, prevents quick deployment and use, and is an inefficient use of battery power. To solve these problems, the main control board was re–designed and a Hall effect switch (AH180–SNG–7) was incorporated to turn the robot on or off with a magnet held external to the robot.

The main control board is small (30.4 mm by 11.2 mm) and was already filled with components, so several redundant or unused components were removed or rearranged to make space for the Hall effect switch. Labeled photographs of both sides of the main control board before the modifications are shown in Figure 2.2. One of the two FPC connectors and the external crystal oscillator were removed from the board. The package for the MCU was replaced with a smaller one and was programed to use an internal crystal oscillator. Also, the single–output voltage regulator was replaced with a dual–output voltage regulator (TPS719285–285) so that the power connection for the MCU could be separate from the one for the RF transceiver and the motor driver. A labeled electrical schematic showing the implementation of the Hall effect switch and dual–output regulator is presented in Figure 10.1.

The dual–output regulator and the Hall effect switch are both powered directly by the battery (V+ and V-). The output pin of the Hall effect switch (OUT) was connected to the

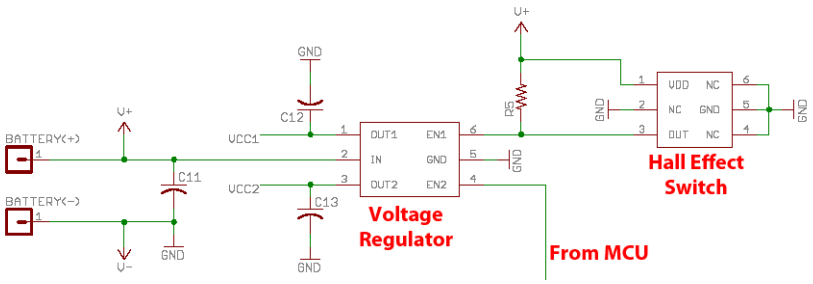

Figure 10.1: Electrical Schematic Showing Implementation of Hall Effect Switch and Dual–Output Regulator

first enable pin on the voltage regulator (EN1). Because the MCU's power line (VCC1) was connected to the corresponding output pin (OUT1) for EN1 on the voltage regulator, the Hall effect switch controls the on/off state of the MCU. A general input/output (I/O) pin on the MCU was connected to the second enable pin on the voltage regular (EN2) and the power lines of the RF transmitter and motor driver (VCC2) were connected to the output pin on the voltage regulator (OUT2) corresponding to EN2. When the MCU is powered on, it can turn the RF transmitter and motor driver on or off by setting this I/O line high or low. With this connection scheme, the entire control board (except the voltage regulator and Hall effect switch) can be powered off by holding magnet near the Hall effect switch when the robot is fully assembled. Without a magnet near the Hall effect switch, the MCU is powered on and the state of the MCU's I/O pin connected to EN2 controls the power to the RF transceiver and the motor driver.

The addition of the Hall effect switch allows for assembly and testing prior to use and storage at an extremely low power state. Through *ex vivo* testing, it was confirmed that the redesign of the main control board and implementation of the Hall effect switch were successful. During the course of these tests, a robot was powered on and off daily for a period of two months. A programmed initialization routine tested the motors during the power up procedure. Over the course of the two months, the robot continued to function properly.

10.2 In–Circuit Serial Programming

As discussed in Section 2.2, another limitation of the modular robot was that the correct software had to be programmed to the MCU before soldering it to the main control board. If errors existed in the code or if new functionality was to be added, a completely new board had to be used. To overcome this problem, the dual–output voltage regulator was used along with the remaining six–pin FPC connector to take advantage of the MCU's in–circuit serial programming (ICSP) capabilities. A voltage regulator with dual–outputs was needed to separate the power pins on the MCU from those on the RF transceiver and motor driver. This is because during ICSP, voltage levels are reached that are higher than the maximum allowed on the RF transceiver and motor driver. Also, the pins attached to the six–pin FPC connector were chosen carefully so that the sensor payload could still utilize this connector.

With the update to the main control board, it was verified through *ex vivo* testing that the software for the microprocessor can now be changed by using the six–pin FPC connector. In turn, this allows for immediate implementation of updated program code, greater flexibility in the development of new payloads, and adoption of microprocessor features such as power saving functions. Photographs and a full electrical schematic of the updated main control board are shown in Figure 10.2 and Appendix A, respectively.

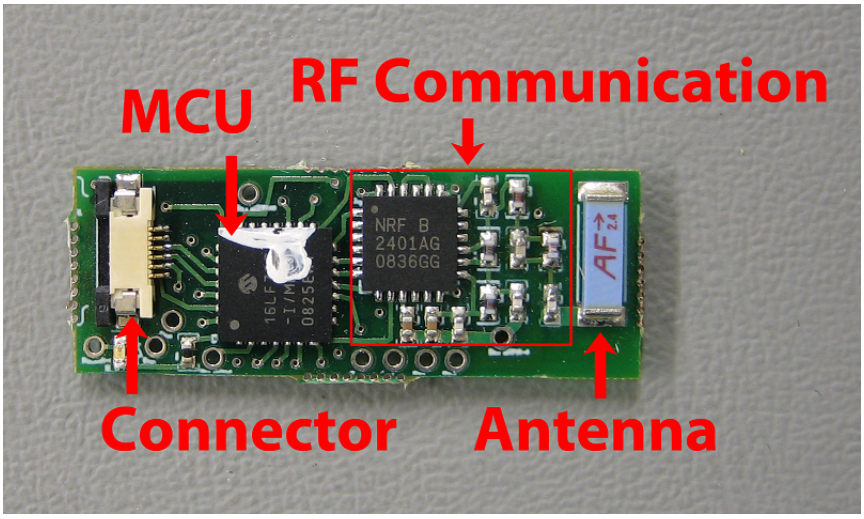

(a)

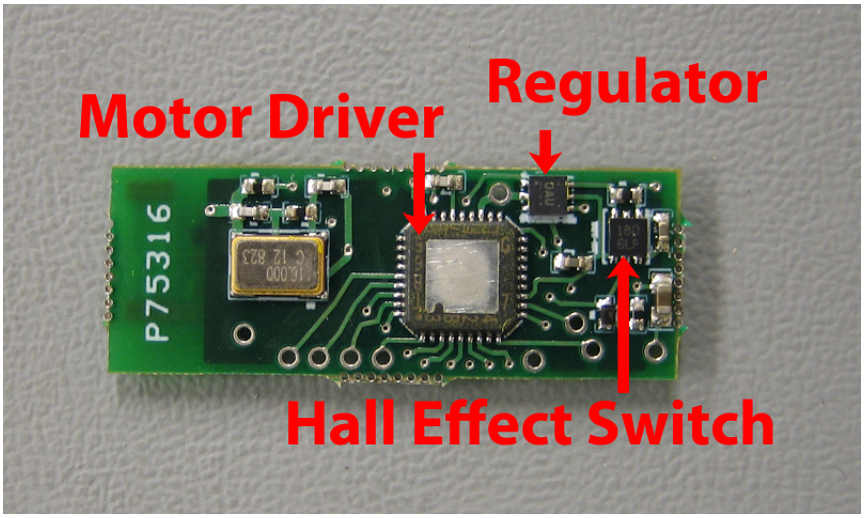

(b)

Figure 10.2: Updated Main Control Board: (a) Front and (b) Back

Chapter 11

Conclusions

Miniature, incorporeal robotic assistants represent a potentially innovative solution to the limited access and multiple incision problems associated with minimally invasive abdominal surgery. Previous work had demonstrated that a family of fixed–base and a family of modular, wireless incorporeal mobile robots could successfully operate within the abdominal cavity. However, the family of modular robots did not have a payload with the ability to store and dispense liquids.

The main focus of this thesis was the development of a liquid drug delivery payload for this family of robotic assistants. Included in the development was a method for mixing two liquids stored inside the robot as they are dispensed, which is needed for dual compound liquids such as fibrin sealants. In addition, two improvements to the current design of the main circuit board were presented that allow for more rapid robot deployment and provide the ability for point of use changes to the embedded control software.

Based on the three general design requirements for having a liquid drug delivery payload:

1. A sealed chamber that can separately store two different liquids,
2. A mechanism to dispense the liquids in the chamber, and
3. An ability to mix the two liquids stored in the chamber before they are dispensed (e.g., if fibrin sealant is used),

a prototype concept was designed, built, and tested. A liquid reservoir built into the robot payload body was shown to be leak–free through bench–top and porcine model testing. The motor, 256:1 gearhead, and leadscrew mechanism for the liquid delivery payload were shown to be more than adequate to actuate the plunger while keeping a leak–free seal. Different

hoses were attached to the reservoir that could simply deliver liquid or could also mix two liquids stored in the reservoir as they are dispensed. A static mixer was incorporated into the hose to provide this mixing. A color dilution experiment was set up and conducted to verify mixing results from ANSYS Fluent 12.1 CFD simulations. Once verified, additional configurations were explored using simulation, and an SMX style hose design was found to produce the highest degree of mixing of the group tested. Two incorporeal robots with a liquid delivery payload and SMX style mixing hose were assembled, shipped to the University of Colorado, and tested in a porcine model. After shipping and five days of storage, the robots were found to be leak–free. The robots successfully dispensed liquid from the reservoirs to the internal organs of the porcine.

Finally, the robot's main circuit board was redesigned. A Hall effect switch was added that allowed an external magnet to disconnect power from the robot. This improvement allows for assembly and testing prior to use, and long–term storage at an extremely low power state. Also with the redesign of the circuit board, in–circuit serial programing capabilities were added. This improvement allows for immediate implementation of updated embedded control software, greater flexibility in the development of new payloads, and adoption of microprocessor features such as power saving functions. Through *ex vivo* testing, it was confirmed that the redesign of the main control board, implementation of the Hall effect switch, and implementation of in–circuit serial programming were successful.

Appendix A

Main Control Board Schematic

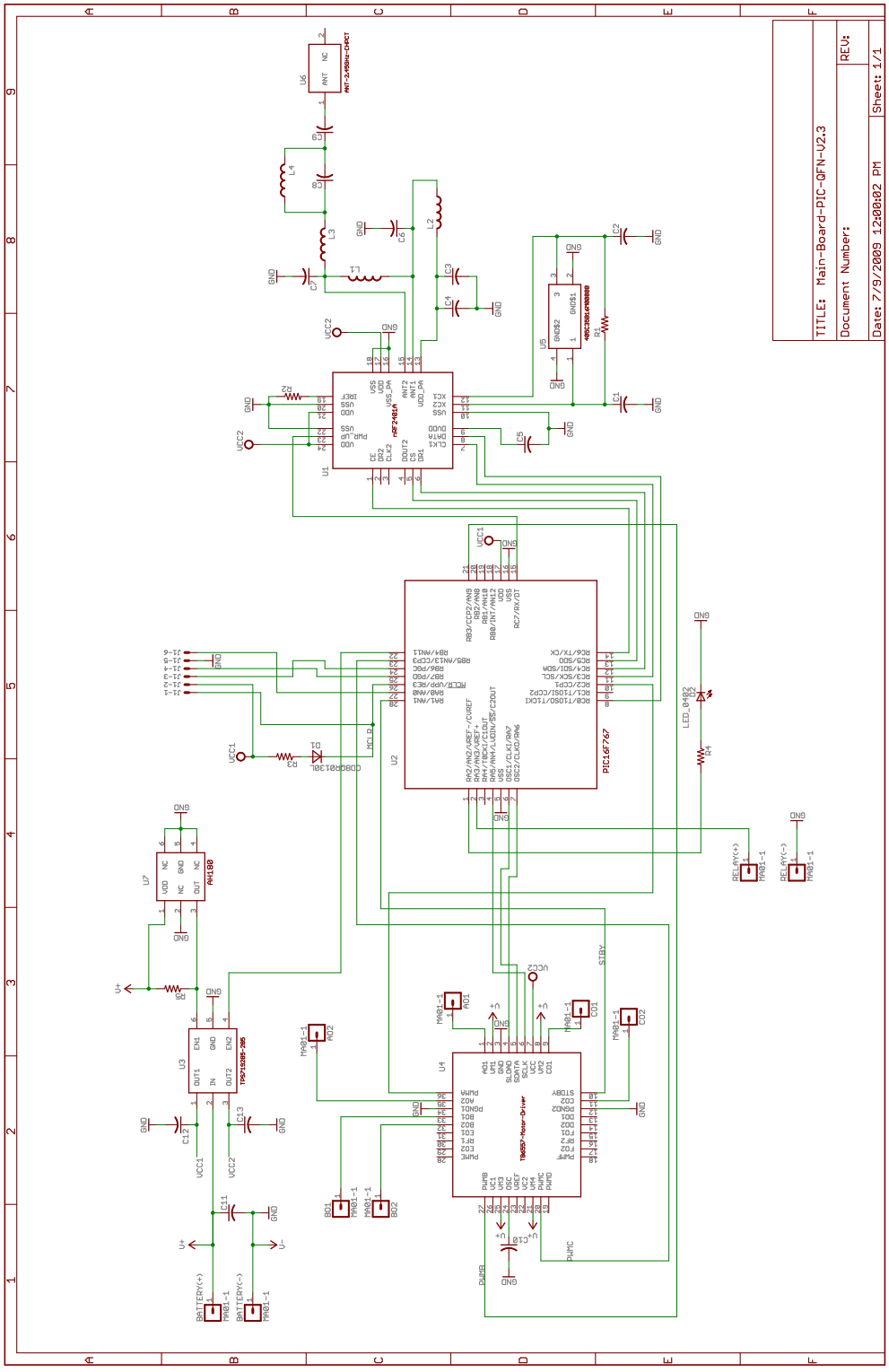

Figure A.1: Full Electrical Schematic of Updated Main Control Board

References

[1] "Minimally invasive surgery," 2010, Mayo Foundation for Medical Education and Research. [Online]. Available: http://www.mayoclinic.org/minimally-invasive-surgery/

[2] M. J. Mack, "Minimally invasive and robotic surgery," *The Journal of the American Medical Association*, vol. 285, pp. 568–572, Feb. 2001.

[3] A. Cuschieri, "Technology for minimal access surgery," *British Medical Journal*, vol. 319, pp. 1–6, Nov. 1999.

[4] E. Boyle, P. F. Ridgway, F. B. Keane, and P. Neary, "Laparoscopic colonic resection in inflammatory bowel disease: Minimal surgery, minimal access and minimal hospital stay," *Colorectal Disease*, vol. 10, no. 9, pp. 911–915, 2008.

[5] M. A. Ströhlein, K.-U. Grützner, K.-W. Jauch, and M. M. Heiss, "Comparison of laparoscopic vs. open access surgery in patients with rectal cancer: A prospective analysis," *Journal of Laparoendoscopic and Advanced Surgical Techniques*, vol. 51, pp. 385–391, Apr. 2008.

[6] V. Nakhamiyayev, L. Galldin, M. Chiarello, A. Lumba, , and P. J. Gorecki, "Laparoscopic appendectomy is the preferred approach for appendicitis: a retrospective review of two practice patterns," *Surgical Endoscopy*, vol. 24, no. 4, pp. 859–864, Apr. 2010.

[7] J. E. Varela, S. E. Wilson, and N. T. Nguyen, "Laparoscopic surgery significantly reduces surgical-site infections compared with open surgery," *Surgical Endoscopy*, vol. 24, no. 2, pp. 270–276, Feb. 2010.

[8] A. R. Lanfranco, A. E. Castellanos, J. P. Desai, and W. C. Meyers, "Robotic surgery: A current perspective," *Annals of Surgery*, vol. 239, no. 1, pp. 14–21, Jan. 2004.

[9] J. R. Romanelli and D. B. Earle, "Single-port laparoscopic surgery: an overview," *Surgical Endoscopy*, vol. 23, no. 7, pp. 1419–1427, July 2009.

[10] J. P. Pearl and J. L. Ponsky, "Natural orifice translumenal endoscopic surgery: A critical review," *Journal of Gastrointestinal Surgery*, vol. 12, no. 7, pp. 1293–1300, 2008.

[11] "FAQ," 2010, Natural Orifice Surgery Consortium for Assessment and Research. [Online]. Available: http://www.noscar.org/faq.php

[12] S. Horgan et al., "Natural orifice surgery: initial clinical experience," *Surgical Endoscopy*, vol. 23, no. 7, pp. 1512–1518, 2009.

[13] M. C. Çavuşoğlu, W. Williams, F. Tendick, and S. S. Sastry, "Robotics for telesurgery: Second generation Berkeley/UCSF laparoscopic telesurgical workstation and looking towards the future applications," *Industrial Robot*, vol. 30, no. 1, pp. 22–29, 2003.

[14] M. C. Çavuşoğlu and S. S. Sastry, "Telesurgery and surgical simulation: Haptic interfaces to real and virtual surgical environments," in *In Touch in Virtual Environments, Ser, IMSC Series in Multimedia*, 2001, pp. 217–237.

[15] W. Ang, "Active tremor compensation in handheld instrument for microsurgery," Carnegie Mellon University Robotics Institute, Pittsburg, PA, Ph.D dissertation SMU-RI-TR-04-28, 2004.

[16] C. N. Riviere, W. T. Ang, and P. K. Khosla, "Toward active tremor canceling in handheld microsurgical instruments," *IEEE Transactions on Robotics and Automation*, vol. 19, no. 5, pp. 793–800, Oct. 2003.

[17] J. Rosen, M. Lum, D. Trimble, B. Hannaford, and M. Sinanan, "Spherical mechanism analysis of a surgical robot for minimally invasive surgery - analytical and experimental approaches," *Studies in Health Technology and Informatics*, vol. 111, pp. 422–428, 2005.

[18] R. H. Taylor, J. Funda, B. Eldridge et al., "A telerobotic assistant for laparoscopic surgery," *IEEE Engineering in Medicine and Biology Magazine*, vol. 14, no. 3, pp. 279–288, May 1995.

[19] J. Sackier and Y. Wang, "Robotically assisted laparoscopic surgery: From concept to development," *Surgical Endoscopy*, vol. 8, no. 1, pp. 63–66, Jan. 1994.

[20] F. Corcione, C. Esposito, D. Cuccurullo, A. Settembre, N. Miranda, F. Amato, F. Pirozzi, and P. Caiazzo, "Advantages and limits of robot-assisted laparoscopic surgery: preliminary experience," *Surgical Endoscopy*, vol. 19, no. 1, pp. 117–119, Jan. 2005.

[21] S. Breitenstein, A. Nocito, M. Puhan, U. Held, M. Weber, and P.-A. Clavien, "Robotic-assisted versus laparoscopic cholecystectomy: Outcome and cost analyses of a case-matched control study," *Annals of Surgery*, vol. 247, no. 6, pp. 987–993, June 2008.

[22] B. P. Müller-Stich, M. A. Reiter, M. N. Wente, V. V. Bintintan, J. Köninger, M. W. Büchler, and C. N. Gutt, "Robot-assisted versus conventional laparoscopic fundoplication: short-term outcome of a pilot randomized controlled trial," *Surgical Endoscopy*, vol. 21, no. 10, pp. 1800–1805, Oct. 2007.

[23] A. Glukhovsky and H. Jacob, "The development and application of wireless capsule endoscopy," *Int. J. Med. Robot. Computer. Assisted Surgery*, vol. 1, pp. 114–123, 2004.

[24] G. Meron, "The development of the swallowable video capsule," *Gastrointestinal Endoscopy*, vol. 6, pp. 817–819, 2000.

[25] M. Simi, P. Valdastri, C. Quaglia, A. Menciassi, and P. Dario, "Design, fabrication, and testing of a capsule with hybrid locomotion for gastrointestinal tract exploration," *IEEE/ASME Transactions on Mechatronics*, vol. 15, no. 2, pp. 170–180, Apr. 2010.

[26] A. Miller, P. Allen, and D. Fowler, "In–vivo stereoscopic imaging system with 5 degrees-of-freedom for minimal access surgery," *Studies in Health Technology and Informatics*, vol. 98, pp. 234–240, 2004.

[27] D. L. Fowler, T. Hu, T. Nadkarni, P. K. Allen, and N. J. Hogle, "Initial trial of a stereoscopic, insertable, remotely controlled camera for minimal access surgery," *Surgical Endoscopy*, vol. 24, no. 1, pp. 9–15, Jan. 2010.

[28] N. A. Patronik, T. Ota, M. A. Zenati, and C. N. Riviere, "A miniature mobile robot for navigation and positioning on the beating heart," *IEEE Transactions on Robotics*, vol. 25, no. 5, pp. 1109–1124, Oct. 2009.

[29] T. Ota, N. A. Patronik, D. Schwartzman, C. N. Riviere, and M. A. Zenati, "Minimally invasive epicardial injections using a novel semiautonomous robotic device," *Circulation*, vol. 118, pp. S115–S120, 2008.

[30] T. Ota, N. A. Patronik, D. Schwartzman, C. N. Riviere, and M. A. Zenati, "Subxiphoid epicardial pacing lead implantation using a miniature crawling robotic device," *Journal of Surgical Research*, vol. 137, pp. 242–243, 2007.

[31] M. Rentschler, A. Hadzialic, J. Dumpert, S. R. Platt, S. Farritor, and D. Oleynikov, "*In vivo* robots for laparoscopic surgery," *Studies in Health Technology and Informatics*, vol. 98, pp. 316–322, 2004.

[32] M. Rentschler, J. Dumpert, S. R. Platt, S. Farritor, and D. Oleynikov, "Mobile *in vivo* camera robots provide sole visual feedback for abdominal exploration and cholecystectomy," *Surgical Endoscopy*, vol. 20, no. 1, pp. 135–138, Jan. 2006.

[33] M. Rentschler, J. Dumpert, S. R. Platt, K. Iagnemma, D. Oleynikov, and S. Farritor, "An *in vivo* mobile robot for surgical vision and task assistance," *ASME Journal of Medical Devices*, vol. 1, no. 1, pp. 23–29, Mar. 2007.

[34] M. E. Rentschler, S. R. Platt, K. Berg, J. Dumpert, D. Oleynikov, and S. M. Farritor, "Miniature *in vivo* robots for remote and harsh environments," *IEEE Transactions on Information Technology in Biomedicine*, vol. 12, no. 1, pp. 66–75, Jan. 2008.

[35] M. E. Rentschler, J. Dumpert, S. R. Platt, S. M. Farritor, and D. Oleynikov, "Natural orifice surgery with an endoluminal mobile robot," *Surgical Endoscopy*, vol. 21, no. 7, pp. 1212–1215, July 2007.

[36] S. R. Platt, J. A. Hawks, and M. Rentschler, "Vision and tasks assistance using modular wireless *in vivo* surgical robots," *IEEE Transactions on Biomedical Engineering*, vol. 56, pp. 1700–1710, June 2009.

[37] M. Rentschler, K. Iagnemma, and S. Farritor, "Mechanical design of robotic *in vivo* wheeled mobility," *ASME Journal of Mechanical Design*, vol. 129, no. 10, pp. 1037–1045, Oct. 2007.

[38] M. Rentschler, J. Dumpert, S. R. Platt, K. Iagnemma, D. Oleynikov, and S. M. Farritor, "Modeling, analysis, and experimental study of *in vivo* wheeled robotic mobility," *IEEE Transactions on Robotics*, vol. 22, no. 2, pp. 308–321, Apr. 2006.

[39] L. A. Evans and A. F. Morey, "Hemostatic agents and tissue glues in urologic injuries and wound healing," *Urologic Clinics of North America*, vol. 33, no. 1, pp. 1–12, Feb. 2006.

[40] T. W. Jarrett, D. Y. Chan, T. C. Charambura, O. Fugita, and L. R. Kavoussi, "Laparoscopic pyeloplasty: The first 100 cases," *Journal of Urology*, vol. 167, no. 3, pp. 1253–1256, Mar. 2002.

[41] A. C. Hindmarsh, E. Cheong, M. P. N. Lewis, and M. Rhodes, "Attendance at a pain clinic with severe chronic pain after open and laparoscopic inguinal hernia repairs," *British Journal of Surgery*, vol. 90, no. 9, pp. 1152–1154, Sep. 2003.

[42] N. Katkhouda et al., "Use of fibrin sealant for prosthetic mesh fixation in laparoscopic extraperitoneal inguinal hernia repair," *Annals of Surgery*, vol. 233, no. 1, pp. 18–25, Jan. 2001.

[43] W. K. Johnston, J. S. Montgomery, B. D. Seifman, B. K. Hollenbeck, and J. S. W. JR, "Fibrin glue v sutured bolster: Lessons learned during 100 laparoscopic partial nephrectomies," *The Journal of Urology*, vol. 174, no. 1, pp. 47–52, July 2005.

[44] R. Patel, R. P. Caruso, S. Taneja, and M. Stifelman, "Use of fibrin glue and gelfoam to repair collecting system injuries in a porcine model: Implications for the technique of laparoscopic partial nephrectomy," *Journal of Endourology*, vol. 17, no. 9, pp. 799–804, Nov. 2003.

[45] M. L. Saxton, "Hemostasis in minimally invasive liver surgery," *Surgery*, vol. 142, no. 4, pp. S46–S49, Oct. 2007.

[46] C. H. Klingler, M. Remzi, M. Marberger, and G. Janetschek, "Haemostasis in laparoscopy," *European Urology*, vol. 50, no. 5, pp. 948–957, Nov. 2006.

[47] R. A. de la Torre, S. L. Bachman, A. A. Wheeler, K. N. Bartow, and J. S. Scott, "Hemostasis and hemostatic agents in minimally invasive surgery," *Surgery*, vol. 142, no. 4, pp. S39–S45, Oct. 2007.

[48] L. P. Msezane, M. H. Katz, O. N. Gofrit, A. L. Shalhav, and K. C. Zorn, "Hemostatic agents and instruments in laparoscopic renal surgery," *Journal of Endourology*, vol. 22, no. 3, pp. 403–408, Mar. 2008.

[49] J.-B. Lattouf, A. Beri, C. H. Klinger, S. Jeschke, and G. Janetschek, "Practical hints for hemostasis in laparoscopic surgery," *Minimally Invasive Therapy and Allied Technologies*, vol. 16, no. 1, pp. 45–51, 2007.

[50] W. D. Spotnitz, "Active and mechanical hemostatic agents," *Surgery*, vol. 142, no. 4, pp. S34–S38, Oct. 2007.

[51] R. Thakur, C. Vial, K. Nigam, E. Nauman, and G. Djelveh, "Static mixers in the process industries – a review," *Chemical Engineering Research and Design*, vol. 81, no. 7, pp. 787–826, Aug. 2003.

[52] "Kenics KM static mixers," 2010, Chemineer. [Online]. Available: http://www.chemineer.com/kenics_km_static_mixers.php

[53] "Flyer SMX plus e," 2010, Sulzer Chemtech. [Online]. Available: http://www.sulzerchemtech.com/en/portaldata/11/Resources//brochures/mrt/Flyer_SMX_plus_e.pdf

[54] M. H. Pahl and E. Muschelknautz, "Static mixers and their applications," *International Chemical Engineering*, vol. 22, no. 2, pp. 197–205, Apr. 1982.

[55] K. J. Myers, A. Bakker, and D. Ryan, "Avoid agitation by selecting static mixers," *Chemical Engineering Progress*, vol. 93, no. 6, pp. 28–38, June 1997.

[56] J. C. Godfrey, "Static mixers," in *Mixing in the Process Industries*, ser. Butterworths Series in Chemical Engineering. London: Butterworth, 1985, ch. 13, pp. 226–250.

[57] P. V. Danckwerts, "The definition and measurement of some characteristics of mixtures," *Applied Scientific Research*, vol. 3, no. 4, pp. 279–296, July 1952.

[58] P. M. C. Lacey, "The mixing of solid particles," *Transactions of the Institution of Chemical Engineers*, vol. 21, pp. 53–59, 1943.

[59] D. Bothe, "Evaluating the quality of a mixture: Degree of homogeneity and scale of segregation," in *Micro and Macro Mixing: Analysis, Simulation and Numerical Calculation*, ser. Heat and Mass Transfer. New York: Springer-Verlag Berlin Heidelberg, 2010, pp. 17–35.

[60] A. Lehwald, D. Thévenin, and K. Zähringer, "Quantifying macro-mixing and micro-mixing in a static mixer using two-tracer laser-induced fluorescence," *Experiments in Fluids*, vol. 48, no. 5, pp. 823–836, May 2010.

[61] A. Lehwald, S. Leschka, D. Thévenin, and K. Zähringer, "Experimental investigation of a static mixer for validation of numerical simulations," in *Micro and Macro Mixing: Analysis, Simulation and Numerical Calculation*, ser. Heat and Mass Transfer. New York: Springer-Verlag Berlin Heidelberg, 2010, pp. 227–243.

[62] R. Wadley and M. Dawson, "LIF measurements of blending in static mixers in the turbulent and transitional flow regimes," *Chemical Engineering Science*, vol. 60, no. 8, pp. 2469–2478, Apr. 2005.

[63] J. Lee and S. Kwon, "Mixing efficiency of a multilamination micromixer with consecutive recirculation zones," *Chemical Engineering Science*, vol. 64, no. 6, pp. 1223–1231, Mar. 2009.

[64] S. W. Lee, D. S. Kim, S. S. Lee, and T. H. Kwon, "A split and recombination micromixer fabricated in a pdms three-dimensional structure," *Journal of Micromechanics and Microengineering*, vol. 16, no. 5, pp. 1067–1072, May 2006.

[65] J. M. Zalc, E. S. Szalai, F. J. Muzzio, and S. Jaffer, "Characterization of flow and mixing in an SMX static mixer," *AIChE Journal*, vol. 48, no. 3, pp. 427–436, Apr. 2003.

[66] "Evicel fibrin sealant (human)," Package Insert, Johnson & Johnson, Somerville, NJ, 2003.

[67] B. R. Munson, D. F. Young, and T. H. Okiishi, *Fundamentals of Fluid Mechanics*, 5th ed. New Jersey: John Wiley & Sons, Inc., 2006.

[68] N.-S. Cheng, "Formula for the viscosity of a glycerol–water mixture," *Industrial and Engineering Chemistry Research*, vol. 47, no. 9, p. 32853288, May 2008.